MOT-based Lifetime Measurements of Potassium-39 $5p_{1/2}$ and $5p_{3/2}$ states

Huan Q. Bui

A thesis presented to the faculty of the

Department of Physics and Astronomy at

Colby College

Department of Physics and Astronomy

Colby College

Waterville, ME

May, 2021

ABSTRACT.

This thesis presents measurements of the lifetimes of $5p_{1/2}$ and $5p_{3/2}$ of ^{39}K via exciting a cloud of ^{39}K atoms in a magneto-optical trap by a linearly-polarized pulse of 405 nm light followed polarization-specific, time-resolved fluorescence detection. We find that $\tau_{5P_{1/2}} = 138.8 \pm 1.6$ ns, which is consistent with past measurements [1], [2] and calculations [3]. The $\tau_{5P_{3/2}}$ measurement is naturally more involved since quantum beats due to hyperfine and Zeeman effect are present. Our observation of $\tau_{5P_{3/2}} = 137.6 \pm 3.1$ ns and $\tau_{5P_{3/2}} = 136.0 \pm 2.4$ ns, obtained from two slightly different approaches, are compared against past measurements [2], [4], [5], [6] and theoretical calculations in [3]. We determine that future work is needed to reduce the uncertainty in our measurement and resolve the discrepancy in the literature.

ACKNOWLEDGMENTS.

Contents

List of Figures

List of Tables

9

1 Introduction

1.1 Motivation

Non-hydrogenic atomic species such as potassium-39 have electronic structures which can introduce anomalous physical effects and complicate ab initio calculations of their reduced matrix elements, which are directly related to many physical properties such as radiative lifetimes of quantum states, hyperfine constants, and polarizabilities. As a result, lifetime measurements, among empirical determinations of these atomic properties, are fundamental for the understanding of atomic structure and provide benchmarks for theorists to improve the robustness of semi-empirical computational methods. A notable example is [13] in which lifetime measurements were performed on francium-223, a highly radioactive element with a half-life of only about 22 minutes, to directly extract the absolute values of certain reduced matrix elements. Due to works such as [14], [13], [2] and others, developments in high-accuracy ab initio calculations could take place and bring theoretical observations and experimental data to better agreement. In the context of this thesis, we consider theoretical results in [3] potassium-39. Table 1 shows the values measured and calculated for the lifetime of $5p_{1/2}$ state of ^{39}K in the literature.

While Table 1 shows good agreement between the most recent theory and measurements, there is a discrepancy of up to 15% on the lifetime of the $5p_{3/2}$ state of potassium-39 in the literature. Table 2 shows the timeline of calculated and measured values for this lifetime. The discrepancy here can be attributed to the fact that the $5p_{3/2} \rightarrow 4s_{1/2}$ decay profile has complex time modulations due to hyperfine and Zeeman quantum beats to be discussed in Section 2 and Appendix 6.1. In addition, the hyperfine splittings $\Delta\nu_{\text{hfs}}$ within the $5p_{3/2}$ state are comparable to $1/\tau_{5p_{3/2}}$, making experimentally eliminating quantum beats and statistical analysis particularly challenging. In the case of the $5p_{1/2} \rightarrow 4s_{1/2}$ decay profile, however, there is little discrepancy in the literature because this decay does not suffer from quantum beats, resulting in substantially smaller systematic errors and more straightforward experimental design.

Author(s)	Year	Method	Lifetime (ns)
Theodosiou [15]	1984	theory	127.06
Safronova et al. [3]	2008	theory	137.2
Berends et al. [2]	1988	experiment (vapor cell)	137 ± 2
Mills et al. [1]	2005	experiment (MOT + ionization)	137.6 ± 1.3

Table 1: Timeline of measurements of the $5p_{1/2}$ state lifetime and their methods.

Author(s)	Year	Method	Lifetime (ns)
Theodosiou [15]	1984	theory	124.02
Safronova et al. [3]	2008	theory	134.0
Schmieder et al. [6]	1968	experiment (level crossing)	140.8 ± 1.0
Ney et al. [5]	1969	experiment (level crossing)	120 ± 4
Svanberg et al. [4]	1971	experiment (level crossing)	133 ± 3
Berends et al. [2]	1988	experiment (vapor cell)	134 ± 2

Table 2: Timeline of measurements of the $5p_{3/2}$ state lifetime and their methods.

1.2 Layout

This work aims to measure the lifetimes of the $5p_{1/2}$ and $5p_{3/2}$ states of potassium-39 using a MOT-based time-resolved fluorescence measurement. The upcoming sections are laid out as follows. Section 2 provides the theoretical background for the experiment. This includes the formula for lifetimes of hyperfine levels, a discussion of the Zeeman effect, and finally a rather extensive treatment of quantum beat theory in radiative lifetime measurements, where we cover only quantum beats due to hyperfine splittings in the absence of external magnetic fields. Section 3.1 describes our experimental procedure and apparatus and reviews previous measurements of $\tau_{5p_{1/2}}$ and $\tau_{5p_{3/2}}$. Section 4 discusses systematic errors and reports our measurement of $\tau_{5p_{1/2}}$, as well as covers the technical difficulties we encountered in the $5p_{3/2}$ measurement and suggests methods to overcome these chal-

lenges. Finally, the Appendix discusses quantum beat theory in the density matrix formalism and lays out the basics of graphical method for angular momentum algebra, which was used extensively in the quantum theory calculation.

2 Theoretical Background

2.1 Lifetime of hyperfine levels

The radiative lifetime of a quantum state can be described by Fermi's golden rule. In the dipole approximation, the decay rate vacuum Γ_{fi} between levels $\{|f\rangle\}$ and $\{|i\rangle\}$ is related to the matrix element between those states by the following expression:

$$\frac{1}{\tau_{fi}} = \Gamma_{fi} = \frac{\omega_0^3}{3\pi\epsilon_0\hbar c^3}|\langle f|\, e\mathbf{r}\,|i\rangle|^2 = \frac{4\alpha\omega_0^3}{3c^2}|\langle f|\, e\mathbf{r}\,|i\rangle|^2,$$

where τ_{fi} is the lifetime, ω_0 is the emission frequency, $\langle f|\, e\mathbf{r}\,|i\rangle$ is the transition dipole moment (for dipole moment operator $e\mathbf{r}$ where e is the elementary charge and $\mathbf{r}$ is the position operator), $\hbar$ is the reduced Planck's constant, c is the speed of light in vacuum, and α is the fine-structure constant. To be more explicit, we may also write

$$\frac{1}{\tau_{fi}} = \Gamma_{fi} = \sum_q \frac{\omega_0^3}{3\pi\epsilon_0\hbar c^3}\left|\langle f|\, er_q^{(1)}\,|i\rangle\right|^2$$

where the r_q's are spherical tensor operators.

Since one is often interested in measuring the decay rate between fine- or hyperfine-structure levels, it is useful to express the transition dipole moment matrix element in terms of the quantum numbers such as n, J, m_J or n, J, F, m_F. The fine-structure splitting is due to the interaction between the electron's orbital angular momentum L and its spin S, giving the quantum number J, where $\mathbf{J} = \mathbf{L} + \mathbf{S}$, and its associated magnetic sublevels m_J. For the states $\{|f\rangle\} = \{|nJm_J\rangle\}$ and $\{|i\rangle\} = \{|n'J'm_{J'}\rangle\}$, we can obtain an expression for $A_{JJ'}$ by an application of the Wigner–Eckart theorem

$$\frac{1}{\tau_{JJ'}} = A_{JJ'} = \frac{\omega_0^3}{3\pi\epsilon_0\hbar c^3}\frac{|\langle nJ|\,|e\mathbf{r}|\,|n'J'\rangle|^2}{2J+1},$$

where $\langle nJ|\,|e\mathbf{r}|\,|n'J'\rangle$ is the reduced matrix element, which is not dependent on the magnetic quantum numbers m_J's. Here, the expression is obtained from averaging over the m_J levels in the upper state and summing over the m_J levels in the lower state.

Hyperfine splittings occur when we take into account the coupling between the electron spin S and the nuclear spin I of the atom. This gives the quantum number F in

addition to J, where $\mathbf{F} = \mathbf{J} + \mathbf{I}$. Following standard theory (or see [11]), we can apply the Wigner-Eckhart theorem once more to the reduced matrix element $\langle nJ| |e\mathbf{r}| |n'J'\rangle$ to find the decay rate $A_{Fm_F, F'm_{F'}}$ from $|nJFm_F\rangle$ to $|n'J'F'm_{F'}\rangle$ in terms of the matrix element in n, J only:

$$
\begin{aligned}
A_{Fm_F, F'm_{F'}} &= \frac{\omega_0^3}{3\pi\epsilon_0\hbar c^3} \sum_q \begin{pmatrix} F & 1 & F' \\ -m_F & q & m_{F'} \end{pmatrix}^2 \left| \langle nJF| |e\mathbf{r}| |n'J'F'\rangle \right|^2 \\
&= \frac{\omega_0^3}{3\pi\epsilon_0\hbar c^3} \sum_q \begin{pmatrix} F & 1 & F' \\ -m_F & q & m_{F'} \end{pmatrix}^2 \\
&\qquad \times (2F'+1)(2F+1) \begin{Bmatrix} J & F & I \\ F' & J' & 1 \end{Bmatrix}^2 \left| \langle nJ| |e\mathbf{r}| |n'J'\rangle \right|^2,
\end{aligned}
$$

where () are the Wigner-3j symbols and {} are the Wigner-6j symbols. To obtain the decay $F \to F'$, we average over all m_F sublevels and summing over all $m_{F'}$. The result is

$$
\begin{aligned}
A_{FF'} &= \frac{\omega_0^3}{3\pi\epsilon_0\hbar c^3}(2F'+1) \begin{Bmatrix} J & F & I \\ F' & J' & 1 \end{Bmatrix}^2 \left| \langle nJ| |e\mathbf{r}| |n'J'\rangle \right|^2 \\
&= (2F'+1)(2J+1) \begin{Bmatrix} J & F & I \\ F' & J' & 1 \end{Bmatrix}^2 A_{JJ'}.
\end{aligned}
$$

With this, we see how measuring $\tau_{JJ'}$ allows one to directly obtain all relevant $A_{FF'}$'s. In principle, one gets the same lifetime no matter what sublevel is excited (ignoring quantum beats). Moreover, by summing over all F', we see that all excited states have the same lifetime.

2.2 Zeeman effect

In a static magnetic field, the magnetic sublevels m_F of a given (hyper)fine-structure state are no longer degenerate due to the interaction between electronic spins and the magnetic field. The splitting depends on the atom and the field strength. The extra term in the Hamiltonian due to an external magnetic field has the form

$$
H_B = \frac{\mu_B g_J}{\hbar}(\mathbf{J} + \mathbf{I}) \cdot \mathbf{B},
$$

14

where $\mu_B = e\hbar/2m_e$ is the Bohr magneton and

$$g_J = g_L \frac{J(J+1) - S(S+1) + L(L+1)}{2J(J+1)} + g_S \frac{J(J+1) + S(S+1) - L(L+1)}{2J(J+1)},$$

with g_L, g_S, the Landé factors, determined experimentally.

In the low-field limit, the Hamiltonian takes the form

$$H_{B,\text{weak}} = \frac{\mu_B}{\hbar} g_F \mathbf{F} \cdot \mathbf{B},$$

which implies that F is a good quantum number. As a result, $\{|Fm_F\rangle\}$ are still the eigenstates of the system and can be used to diagonalize this Hamiltonian to find the energy splittings:

$$\Delta E = \mu_B g_F m_F |B|$$

where g_F is a dimensionless strength factor, given by

$$g_F = g_J \frac{F(F+1) - I(J+1) + J(I+1)}{2F(F+1)} + g_I \frac{F(F+1) + I(I+1) - J(J+1)}{2F(F+1)}.$$

For high fields, F is no longer a good quantum number, and the system has eigenstates $\{|Jm_J, Im_I\rangle\}$, where the effects on the orbital electron are much greater than those on the nucleus, rendering the $S - I$ coupling less important. In this case, the Hamiltonian is

$$H_{B,\text{strong}} = \frac{\mu_B}{\hbar} (g_J \mathbf{J} + g_I \mathbf{I}) \cdot \mathbf{B}.$$

Without any assumptions on field strength, we may use $\{|Jm_J, Im_I\rangle\}$ as the basis states to calculate various hyperfine-structure energy shifts due to the Zeeman effect. The general Hamiltonian in this case, which takes into account all effects due to the nuclear spin, is

$$H_B = A_{\text{hfs}} \mathbf{I} \cdot \mathbf{J} + \frac{\mu_B}{\hbar} (g_J \mathbf{J} + g_I \mathbf{I}) \cdot \mathbf{B},$$

where A_{hfs} is a constant characteristic of the atom that is determined experimentally. In the electric quadrupole approximation, this Hamiltonian as a function of magnetic field strength is approximated by

$$H_{\text{hfs}} = A_{\text{hfs}} \mathbf{I} \cdot \mathbf{J} + B_{\text{hfs}} \frac{3(\mathbf{I} \cdot \mathbf{J})^2 + \frac{3}{2}\mathbf{I} \cdot \mathbf{J} - \mathbf{I}^2 \cdot \mathbf{J}^2}{2I(2I-1)J(J-1)} + \frac{\mu_B}{\hbar} (g_J m_J + g_I m_I) B,$$

15
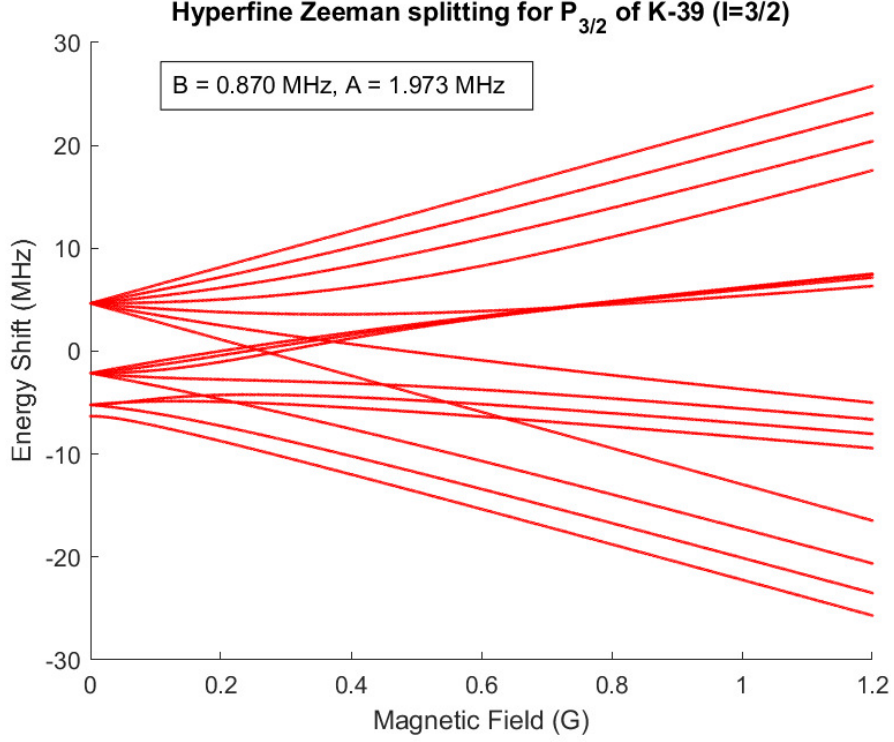
Figure 1: Energy level diagram for a $P_{3/2}$ state in an atom with $I = 3/2$ and hyperfine coefficients A, B taken from measurements due to [4].

where B_{hfs}, along with A_{hfs} and the g-factors, is also an experimentally determined value. As discussed in the preceding paragraphs, this Hamiltonian can be analytically diagonalized in the low- and high-field limits. In general, however, H_{hfs} must be diagonalized numerically using $\{|Jm_J, Im_I\rangle\}$ as the basis states. In this basis, the matrix elements of $\mathbf{I} \cdot \mathbf{J}$ and of $3(\mathbf{I} \cdot \mathbf{J})^2 + \frac{3}{2}\mathbf{I} \cdot \mathbf{J} - \mathbf{I}^2 \cdot \mathbf{J}^2$ are known. The reader may refer to [16], particularly Appendix C, for detailed discussions and calculations. The reader may also refer to [17] for more information. Note that the calculations in [17] are for ^{40}K ($I = 4$), so numerical values and certain level diagrams are different than those for ^{39}K ($I = 3/2$). Figure 1, generated using a MATLAB routine (See Appendix 6.4 for the code), shows schematically the Zeeman splitting within the hyperfine states of $P_{J=3/2}$ as a function of magnetic field strength for an atomic species with $I = 3/2$, with empirical values for A_{hfs} and B_{hfs} taken from [4].

2.3 Quantum beats in radiative lifetime measurements

2.3.1 Introduction

This section details some theory related to quantum beats, which occur in and can affect radiative lifetime measurements. Most of the mathematical ideas can be found in [10], [17], and Section 7.2: Quantum Beat Theory in the Density Matrix Formalism in "Quantum Beats and Time-Resolved Fluorescence Spectroscopy" by S. Haroche in [8]. Appendix 6.1 summarizes some of these ideas.
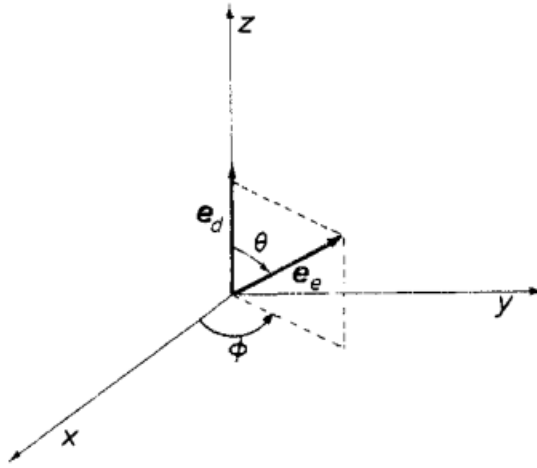
Figure 2: Excitation-detection geometry using linear polarizers [10].

While the underlying mathematical theory of quantum beats is fairly involved, the forthcoming "magic angle solution" allows one to eliminate quantum beats in the experimentally setting in a straightforward manner.

2.3.2 The Magic-Angle Solution [7]

Consider an experiment where atoms are excited with linearly polarized light, and the emitted light passes through a linear polarizer before reaching the detector. The radiation pattern is spatially anisotropic and the polarization depends on the direction of detection relative to the source. In this subsection, we argue that if the polarization vector of the

exciting light forms the "magic angle" θ_m given by:

$$\theta_m = \arccos\left(1/\sqrt{3}\right) \approx 54.74°$$

with the axis of the linear polarizer in front of the detector, then the detected signal is insensitive to the anisotropic part of the fluorescence.

Here we present a *qualitative* magic angle solution due to [7]. A more complete treatment of this problem is outlined in the following sections and appendices. To start, we assume weak and broadline/broadband excitation so that all hyperfine levels are excited. Assume further that the ground state is initially unpolarized. This means that the polarization of the excited state is that of a photon, i.e., in addition to *population*, which is the rank-zero component of the excited state density matrix, there can also be the *orientation* (rank-one) and *alignment* (rank-two) components. For a physical picture of orientation and alignment, the reader may refer to [18]. Now, when the excitation light is linearly polarized, the density matrix of the excited state has no orientation ($k = 1$) component. This leaves us with the population ($k = 0$) and alignment ($k = 2$) terms. As we will see, only the alignment term contributes to radiation anisotropy. This anisotropy corresponds to $k = 2, q = 0$, where k, q correspond to the tensor rank and component, respectively. The Wigner-Eckart theorem leads to the following expression for the radiation intensity:

$$I(\theta, \phi, t) \propto A + B(t)P_2(\cos\theta) = A + B(t)Y_2^0(\theta, \phi)$$

where θ is the angle between the radiated and detected polarization. Here, A and $B(t)$ depends on the system and are not necessarily non-zero. This states that the radiation has no ϕ-dependence, and that quantum beats arise when $P_2(\cos\theta) \neq 0$. When $\theta = \theta_m$, $P_2(\cos\theta)$ vanishes. Discussions of tensor expansions and the details related to this problem can be found below and in [8], [10], [9].

2.3.3   Some quantum-beat theory

Roughly speaking, quantum beats occur due to "interference" in the decay of a coherent superposition of closely-spaced atomic states $\{|e\rangle\}$ to some collection of the final states

$\{|f\rangle\}$, where $\{|e\rangle\}$ is obtained by an pulsed laser with pulse duration $\Theta \ll \tau$, the mean lifetime of $\{|e\rangle\}$. The basic scheme is given by Figure 3.
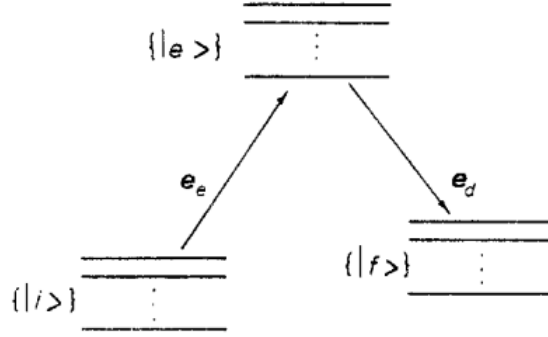
Figure 3: Typical quantum-beat scheme [10].

A short pulse of resonant light of polarization $\mathbf{e}_e$ excites an ensemble of atoms from a set of initial states $\{|i\rangle\}$ to $\{|e\rangle\}$. The decay $\{|e\rangle\} \to \{|f\rangle\}$ generates fluorescence light with intensity $I_{tot}(t)$. We are interested in the intensity $I(t)$ of a particular polarization $\mathbf{e}_d$ of $I_{tot}(t)$. In general (see Appendix 6.1), we have

$$I(t) \propto \mathrm{Tr}_e\{\rho_e(t)\mathfrak{D}\}, \tag{1}$$

where $\rho_e(t)$ is the density matrix of the excited state describing the time evolution of the excited state after the pulse, and $\mathfrak{D}$ is the detection operator given in terms of the scaled-electric-dipole operator $\mathbf{D}$ as

$$\mathfrak{D} = \sum_f (\mathbf{e}_d \cdot \mathbf{D}) |f\rangle \langle f| (\mathbf{e}_d^* \cdot \mathbf{D}), \tag{2}$$

where $\mathbf{e}_d$ is the detection polarization vector. $\rho_e(t)$ is simple so long as the following conditions are satisfied:

- The excitation is broadline, i.e., the spectral width of the exciting light is much bigger than the inverse of the duration of the pulse.

- The excitation is weakly-coupled to the atomic system, i.e., the duration of the pulse is much less than the average time between two successive photon absorptions by an atom.

19

- The duration of the pulse is shorter than the mean lifetime τ of $\{|e\rangle\}$, and is less than the inverse Bohr frequencies $\omega_{e,e'}$ corresponding to the excited-state energy differences.

Under these conditions, the density matrix $\rho_e(t)$ has the following property:

$$\langle e|\,\rho_e(t)\,|e'\rangle = \sum_{ii'} \langle e|\,\mathbf{e}_e \cdot \mathbf{D}\,|i\rangle\,\langle i|\,\rho_i(-T)\,|i'\rangle\,\langle i'|\,\mathbf{e}_e^* \cdot \mathbf{D}\,|e'\rangle \exp\left[-(i\omega_{ee'} + \Gamma_e)t\right], \quad (3)$$

where $\rho_i(-T)$ is the density matrix of the initial state and $\mathbf{e}_e$ is the excitation polarization vector. Here, $\Gamma_e = \tau_e^{-1}$. Putting Eq. 3 into Eq. 1 and Eq. 2 we find

$$I(t) \propto \sum_{f,ii',ee'} \langle e|\,\mathbf{e}_e \cdot \mathbf{D}\,|i\rangle\,\langle i|\,\rho_i(-T)\,|i'\rangle\,\langle i'|\,\mathbf{e}_e^* \cdot \mathbf{D}\,|e'\rangle$$

$$\times \langle e'|\,\mathbf{e}_d \cdot \mathbf{D}\,|f\rangle\,\langle f|\,\mathbf{e}_d^* \cdot \mathbf{D}\,|e\rangle \exp\left[-(i\omega_{ee'} + \Gamma_e)t\right]. \quad (4)$$

This corresponds exactly to Eq. 18 in Appendix 6.1. For a detailed derivation of this equation, the reader may refer to the rest of Appendix 6.1, where the symbol for initial states i becomes g.

2.3.4 Hyperfine-structure quantum beats

Now we focus on quantum beats due to hyperfine splitting, assuming that no splitting due to Zeeman effects are present. The atoms are assumed to have a non-zero nuclear spin. In our case, potassium-30 has $I = 3/2$. The atomic states will be represented by

$$|a\rangle = |\alpha(J_a I) F_a M_a\rangle \equiv |F_a M_a\rangle, \quad a = i, e, f. \quad (5)$$

J_a denotes the total electronic angular momentum, I the nuclear spin, F_a the total angular momentum and M_a the quantum number corresponding to its projection on the z-axis. Finally, α stands for all other labels necessary to identify each state. We assume that initially, the ground state is unpolarized (or, totally mixed), i.e., that $\rho_i(-T) \propto \mathbb{I}$, the identity matrix. In this case, the intensity $I(t)$ measured with polarization $\mathbf{e}_d$ and excited with $\mathbf{e}_e$ is slightly simplified:

$$I(t) \propto \sum_{F_e M_e, F_e' M_e', F_i M_i, F_f M_f} \langle F_e M_e|\,\mathbf{e}_e \cdot \mathbf{D}\,|F_i M_i\rangle\,\langle F_i M_i|\,\mathbf{e}_e^* \cdot \mathbf{D}\,|F_e' M_e'\rangle$$

$$\times \langle F_e' M_e'|\,\mathbf{e}_d \cdot \mathbf{D}\,|F_f M_f\rangle\,\langle F_f M_f|\,\mathbf{e}_d^* \cdot \mathbf{D}\,|F_e M_e\rangle \exp\left[-(i\omega_{F_e F_e'} + \Gamma_e)t\right], \quad (6)$$

where the constant of proportionality includes fundamental and algebraic constants. The next step is to eliminate irrelevant quantum numbers in order to make the dependence on the characteristics of the atom more explicit. To this end, we will eliminate the quantum numbers M_F and sum over all F_i, F_f. Eliminating M_F's requires reducing the electric-dipole matrix elements. We do this by making use of the Wigner-Eckart theorem and known reduction formulas. First, we eliminate the dependence on the M_F quantum numbers by introducing reduced matrix elements and decomposing $\mathbf{e} \cdot \mathbf{D}$ into the tensor components p_0:

$$
\begin{aligned}
\langle F_e M_e | \, \mathbf{e}_e \cdot \mathbf{D} \, | F_i M_i \rangle &= \sum_{p_0} (\mathbf{e}_e)_{p_0} \, \langle F_e M_e | \, \mathbf{D}_{p_0} \, | F_i M_i \rangle \\
&= \sum_{p_0} (\mathbf{e}_e)_{p_0} (-1)^{F_e - M_e}
\begin{pmatrix} F_e & 1 & F_i \\ -M_e & p_0 & M_i \end{pmatrix}
\langle F_e | | \mathbf{D} | | F_i \rangle \\
&= \sum_{p_0} (\mathbf{e}_e)_{p_0} (-1)^{F_e - M_e}
\begin{pmatrix} F_e & 1 & F_i \\ -M_e & p_0 & M_i \end{pmatrix}
\langle (J_e I) F_e | | \mathbf{D} | | (J_i I) F_i \rangle .
\end{aligned}
$$

Similarly,

$$
\begin{aligned}
\langle F_i M_i | \, \mathbf{e}_e^* \cdot \mathbf{D} \, | F_e' M_e' \rangle &= \sum_{p_0'} (\mathbf{e}_e^*)_{p_0'} \, \langle F_i M_i | \, \mathbf{D}_{p_0'} \, | F_e' M_e' \rangle \\
&= \sum_{p_0'} (\mathbf{e}_e^*)_{p_0'} (-1)^{F_i - M_i}
\begin{pmatrix} F_i & 1 & F_e' \\ -M_i & p_0' & M_e' \end{pmatrix}
\langle F_i | | \mathbf{D} | | F_e' \rangle \\
&= \sum_{p_0'} (\mathbf{e}_e^*)_{p_0'} (-1)^{F_i - M_i}
\begin{pmatrix} F_i & 1 & F_e' \\ -M_i & p_0' & M_e' \end{pmatrix}
\langle (J_i I) F_i | | \mathbf{D} | | (J_e I) F_e' \rangle .
\end{aligned}
$$

$$
\begin{aligned}
\langle F_e' M_e' | \, \mathbf{e}_d \cdot \mathbf{D} \, | F_f M_f \rangle &= \sum_{p} (\mathbf{e}_d)_{p} \, \langle F_e' M_e' | \, \mathbf{D}_{p} \, | F_f M_f \rangle \\
&= \sum_{p} (\mathbf{e}_d)_{p} (-1)^{F_e' - M_e'}
\begin{pmatrix} F_e' & 1 & F_f \\ -M_e' & p & M_f \end{pmatrix}
\langle F_e' | | \mathbf{D} | | F_f \rangle \\
&= \sum_{p} (\mathbf{e}_d)_{p_0'} (-1)^{F_e' - M_e'}
\begin{pmatrix} F_e' & 1 & F_f \\ -M_e' & p & M_f \end{pmatrix}
\langle (J_e I) F_e' | | \mathbf{D} | | (J_f I) F_f \rangle
\end{aligned}
$$

$$\langle F_f M_f | \, \mathbf{e}_d^* \cdot \mathbf{D} \, | F_e M_e \rangle = \sum_{p'} (\mathbf{e}_d^*)_{p'} \, \langle F_f M_f | \, \mathbf{D}_{p'} \, | F_e M_e \rangle$$

$$= \sum_{p'} (\mathbf{e}_d^*)_{p'} (-1)^{F_f - M_f} \begin{pmatrix} F_f & 1 & F_e \\ -M_f & p' & M_e \end{pmatrix} \langle F_f | \, |\mathbf{D}| \, | F_e \rangle$$

$$= \sum_{p'} (\mathbf{e}_d^*)_{p'} (-1)^{F_f - M_f} \begin{pmatrix} F_f & 1 & F_e \\ -M_f & p' & M_e \end{pmatrix} \langle (J_f I) F_f | \, |\mathbf{D}| \, | (J_e I) F_e \rangle .$$

Next, we further reduce the matrix elements $\langle (J'I) F' | \, \mathcal{O} \, | (JI) F \rangle$, introducing the $6j$-symbol:

$$\langle (J_e I) F_e | \, |\mathbf{D}| \, | (J_i I) F_i \rangle = (-1)^{J_e + I + F_i + 1} \sqrt{(2F_e + 1)(2F_i + 1)} \begin{Bmatrix} J_e & F_e & I \\ F_i & J_i & 1 \end{Bmatrix} \langle J_e | \, |\mathbf{D}| \, | J_i \rangle$$

$$= (-1)^{J_e + I + F_i + 1} \sqrt{(2F_e + 1)(2F_i + 1)} \begin{Bmatrix} F_e & F_i & 1 \\ J_i & J_e & I \end{Bmatrix} \langle J_e | \, |\mathbf{D}| \, | J_i \rangle ,$$

where we have used symmetry relations of the $6j$-symbol on the last line. Similarly, we find that

$$\langle (J_i I) F_i | \, |\mathbf{D}| \, | (J_e I) F_e' \rangle = (-1)^{J_i + I + F_e' + 1} \sqrt{(2F_i + 1)(2F_e' + 1)} \begin{Bmatrix} F_i & F_e' & 1 \\ J_e & J_i & I \end{Bmatrix} \langle J_i | \, |\mathbf{D}| \, | J_e \rangle .$$

$$\langle (J_e I) F_e' | \, |\mathbf{D}| \, | (J_f I) F_f \rangle = (-1)^{J_e + I + F_f + 1} \sqrt{(2F_e' + 1)(2F_f + 1)} \begin{Bmatrix} F_e' & F_f & 1 \\ J_f & J_e & I \end{Bmatrix} \langle J_e | \, |\mathbf{D}| \, | J_f \rangle .$$

$$\langle (J_f I) F_f | \, |\mathbf{D}| \, | (J_e I) F_e \rangle = (-1)^{J_f + I + F_e + 1} \sqrt{(2F_f + 1)(2F_e + 1)} \begin{Bmatrix} F_f & F_e & 1 \\ J_e & J_f & I \end{Bmatrix} \langle J_f | \, |\mathbf{D}| \, | J_e \rangle .$$

Putting these together, we can write the signal $I(t)$ as

$$I(t) \propto \sum_{\substack{F_e, F_e' \\ pp', p_0 p_0' \\ F_i, F_f}} (-1)^{p_0 + p_0' + p + p' + F_e + F_e' + F_i + F_f} (2F_e + 1)(2F_e' + 1)(2F_i + 1)(2F_f + 1)$$

$$\times (\mathbf{e}_e)_{p_0} (\mathbf{e}_e^*)_{p_0'} (\mathbf{e}_d)_p (\mathbf{e}_d^*)_{p'} \exp\left[-(i\omega_{F_e F_e'} + \Gamma_e)t\right] |\langle J_e| |\mathbf{D}| |J_i\rangle|^2 |\langle J_e| |\mathbf{D}| |J_f\rangle|^2$$

$$\times \begin{Bmatrix} F_e & F_i & 1 \\ J_i & J_e & I \end{Bmatrix} \begin{Bmatrix} F_i & F_e' & 1 \\ J_e & J_i & I \end{Bmatrix} \begin{Bmatrix} F_e' & F_f & 1 \\ J_f & J_e & I \end{Bmatrix} \begin{Bmatrix} F_f & F_e & 1 \\ J_e & J_f & I \end{Bmatrix}$$

$$\times \sum_{\substack{M_e M_e' \\ M_i M_f}} (-1)^{F_e - M_e + F_e' - M_e' + F_i - M_i + F_f - M_f} \begin{pmatrix} F_e & 1 & F_i \\ -M_e & p_0 & M_i \end{pmatrix} \begin{pmatrix} F_i & 1 & F_e' \\ -M_i & p_0' & M_e' \end{pmatrix}$$

$$\times \begin{pmatrix} F_e' & 1 & F_f \\ -M_e' & p & M_f \end{pmatrix} \begin{pmatrix} F_f & 1 & F_e \\ -M_f & p' & M_e \end{pmatrix}. \tag{7}$$

Let

$$X(F_e, F_e', F_i, F_f; p_0, p_0', p, p') = \sum_{\substack{M_e M_e' \\ M_i M_f}} (-1)^{F_e - M_e + F_e' - M_e' + F_i - M_i + F_f - M_f} \begin{pmatrix} F_e & 1 & F_i \\ -M_e & p_0 & M_i \end{pmatrix}$$

$$\times \begin{pmatrix} F_i & 1 & F_e' \\ -M_i & p_0' & M_e' \end{pmatrix} \begin{pmatrix} F_e' & 1 & F_f \\ -M_e' & p & M_f \end{pmatrix} \begin{pmatrix} F_f & 1 & F_e \\ -M_f & p' & M_e \end{pmatrix}.$$

We will simplify this expression, using graphical methods for angular-momentum theory from [9]. Some of the rules used in the following calculation are summarized in Appendix 6.2. From Appendix 6.2.3, we find

$$X(F_e, F_e', F_i, F_f; p_0, p_0', p, p') = \sum_{kq} (2k + 1)(-1)^{q + 2F_f - F_e - F_e'} \begin{pmatrix} 1 & 1 & k \\ p_0 & p_0' & q \end{pmatrix} \begin{pmatrix} 1 & 1 & k \\ p & p' & -q \end{pmatrix}$$

$$\times \begin{Bmatrix} F_i & F_e & 1 \\ k & 1 & F_e' \end{Bmatrix} \begin{Bmatrix} 1 & k & 1 \\ F_e & F_f & F_e' \end{Bmatrix},$$

23

where q are the z-projected quantum numbers of k. Plugging this expression into Eq. 7 we find

$$I(t) \propto \sum_{\substack{F_e, F'_e \ F_i, F_f \\ pp', p_0 p'_0 \\ kq}} \sum (-1)^{q+2F_f+p_0+p'_0+p+p'+F_i+F_f} (2k+1)(2F_e+1)(2F'_e+1)(2F_i+1)(2F_f+1)$$

$$\times (\mathbf{e}_e)_{p_0} (\mathbf{e}_e^*)_{p'_0} (\mathbf{e}_d)_p (\mathbf{e}_d^*)_{p'} \exp\left[-(i\omega_{F_e F'_e} + \Gamma_e)t\right] |\langle J_e|\,|\mathbf{D}|\,|J_i\rangle|^2 |\langle J_e|\,|\mathbf{D}|\,|J_f\rangle|^2$$

$$\times \begin{Bmatrix} F_e & F_i & 1 \\ J_i & J_e & I \end{Bmatrix} \begin{Bmatrix} F_i & F'_e & 1 \\ J_e & J_i & I \end{Bmatrix} \begin{Bmatrix} F'_e & F_f & 1 \\ J_f & J_e & I \end{Bmatrix} \begin{Bmatrix} F_f & F_e & 1 \\ J_e & J_f & I \end{Bmatrix}$$

$$\times \begin{Bmatrix} F_i & F_e & 1 \\ k & 1 & F'_e \end{Bmatrix} \begin{Bmatrix} 1 & k & 1 \\ F_e & F_f & F'_e \end{Bmatrix} \begin{pmatrix} 1 & 1 & k \\ p_0 & p'_0 & q \end{pmatrix} \begin{pmatrix} 1 & 1 & k \\ p & p' & -q \end{pmatrix}.$$

We can simplify this. Notice that the selection rules on the $3j$-symbols require that $p_0 + p'_0 + q = 0 = p + p' - q$. This means that

$$p_0 + p'_0 + p + p' = 0.$$

Moreover, let

$$Y(F_e, F'_e; k)$$

$$= \sum_{F_i} (2F_i+1)(-1)^{2J_e+k+F_e+F'_e+I+J_i+F_i} \begin{Bmatrix} F_e & F_i & 1 \\ J_i & J_e & I \end{Bmatrix} \begin{Bmatrix} F'_e & F_i & 1 \\ 1 & k & F_e \end{Bmatrix} \begin{Bmatrix} I & F_i & J_i \\ 1 & J_e & F'_e \end{Bmatrix}.$$

and

$$Z(F_e, F'_e; k)$$

$$= \sum_{F_f} (2F_f+1)(-1)^{2J_e+k+F_e+F'_e+I+J_f+F_f} \begin{Bmatrix} F'_e & F_f & 1 \\ J_f & J_e & I \end{Bmatrix} \begin{Bmatrix} F_e & F_f & 1 \\ 1 & k & F'_e \end{Bmatrix} \begin{Bmatrix} I & F_f & J_f \\ 1 & J_e & F_e \end{Bmatrix}.$$

To write $I(t)$ in terms of Y, Z, we must perform some permutations within the $6j$-symbols. This brings out some phase factors which we will drop. After multiple simplifications we

24

find

$$I(t) \propto \sum_{\substack{F_e, F_e' \\ pp', p_0 p_0' \\ kq}} (-1)^{q-J_i+J_f}(2k+1)|\langle J_e| |\mathbf{D}| |J_i\rangle|^2$$

$$\times |\langle J_e| |\mathbf{D}| |J_f\rangle|^2 \exp\left[-(i\omega_{F_e F_e'} + \Gamma_e)t\right](2F_e+1)$$

$$\times (2F_e'+1)(\mathbf{e}_e)_{p_0}(\mathbf{e}_e^*)_{p_0'}(\mathbf{e}_d)_p(\mathbf{e}_d^*)_{p'}\begin{pmatrix} 1 & 1 & k \\ p_0 & p_0' & q \end{pmatrix}\begin{pmatrix} 1 & 1 & k \\ p & p' & -q \end{pmatrix} Y(F_e, F_e'; k)Z(F_e, F_e'; k).$$

(8)

The next step is to calculate $Y(F_e, F_e'; k)$ and $Z(F_e, F_e'; k)$, again using graphical methods (see Appendix 6.2.4). We find

$$Y(F_e, F_e'; k) = \begin{Bmatrix} k & J_e & J_e \\ I & F_e & F_e' \end{Bmatrix}\begin{Bmatrix} k & J_e & J_e \\ J_i & 1 & 1 \end{Bmatrix} = \begin{Bmatrix} F_e & F_e' & k \\ J_e & J_e & I \end{Bmatrix}\begin{Bmatrix} 1 & 1 & k \\ J_e & J_e & J_i \end{Bmatrix}$$

and

$$Z(F_e, F_e'; k) = \begin{Bmatrix} k & J_e & J_e \\ I & F_e & F_e' \end{Bmatrix}\begin{Bmatrix} k & J_e & J_e \\ J_f & 1 & 1 \end{Bmatrix} = \begin{Bmatrix} F_e' & F_e & k \\ J_e & J_e & I \end{Bmatrix}\begin{Bmatrix} 1 & 1 & k \\ J_e & J_e & J_f \end{Bmatrix}.$$

Plugging these results back into Eq. 8 we get

$$I(t) \propto (-1)^{J_i-J_f}|\langle J_e| |\mathbf{D}| |J_i\rangle|^2|\langle J_e| |\mathbf{D}| |J_f\rangle|^2$$

$$\times \sum_{\substack{kq \\ F_e F_e'}} (-1)^q E_q^k U_{-q}^k A^k(F_e F_e')B^k(F_e' F_e)\exp\left[-(i\omega_{F_e F_e'} + \Gamma_e)t\right]$$

(9)

where

$$E_q^k = \sqrt{2k+1}\sum_{p_0 p_0'}\begin{pmatrix} 1 & 1 & k \\ p_0 & p_0' & q \end{pmatrix}(\mathbf{e}_e)_{p_0}(\mathbf{e}_e^*)_{p_0'}$$

$$U_{-q}^k = \sqrt{2k+1}\sum_{pp'}\begin{pmatrix} 1 & 1 & k \\ p & p' & -q \end{pmatrix}(\mathbf{e}_d)_p(\mathbf{e}_d^*)_{p'}$$

$$A^k(F_e F_e') = \sqrt{(2F_e+1)(2F_e'+1)}\begin{Bmatrix} F_e & F_e' & k \\ J_e & J_e & I \end{Bmatrix}\begin{Bmatrix} 1 & 1 & k \\ J_e & J_e & J_i \end{Bmatrix}$$

$$B^k(F_e' F_e) = \sqrt{(2F_e+1)(2F_e'+1)}\begin{Bmatrix} F_e' & F_e & k \\ J_e & J_e & I \end{Bmatrix}\begin{Bmatrix} 1 & 1 & k \\ J_e & J_e & J_f \end{Bmatrix}.$$

25

Eq. 9 has all irrelevant quantum number eliminated. All of the excitation and detection polarization characteristics are contained in the terms E_q^k and U_{-q}^k. The terms $A^k(F_e F_e')$ and $B^k(F_e' F_e)$ depend on the atomic quantum numbers and are transition-specific. The exponential term represents quantum beats. We will see that not all transition $J_i - J_e - J_f$ will exhibit quantum beats because $A^k(F_e F_e')$ and/or $B^k(F_e' F_e)$ might vanish.

2.3.5 Example: Linearly-polarized excitation and detection

Now we are ready to consider the excitation/detection angle dependence in the experimental geometry given in Figure 4, which is the geometry of our experiment. Let the
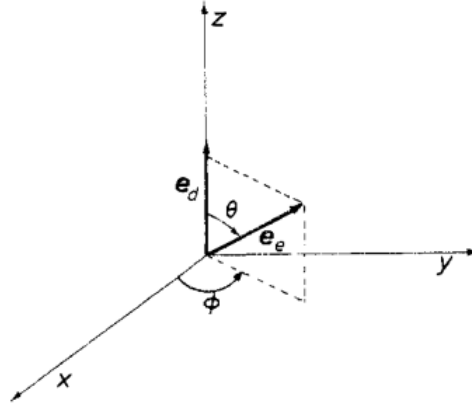
Figure 4: Excitation-detection geometry using linear polarizers [10].

z-axis be defined by the polarization of the detection polarization $\mathbf{e}_d$. The direction of the detection polarization $\mathbf{e}_e$ is defined by the polar angles θ and ϕ. Since we're dealing with on linearly polarized light and a linear polarizer, $p = p' = 0$. Thus, the detection-polarization dependent factor U_{-q}^k takes the form

$$U_{-q}^k = \sqrt{2k+1} \begin{pmatrix} 1 & 1 & k \\ 0 & 0 & 0 \end{pmatrix} \delta_{q0}.$$

We see that $U_{-q}^k = 0$ unless $q = 0$. So, it suffices to find what E_0^k in the lab frame is. To do this, we need some understanding of how the spherical tensor E_q^k transforms under rotations. Specifically, we need to first derive E_q^k in the reference frame x'', y'', z'' making the Euler angles $(0, -\theta, -\phi)$ with the lab frame (this quantity has a similar form as that of

U_{-q}^k). Once this is done, we need to transform E_q^k back into the lab frame. This requires some understanding of the spherical basis, spherical tensors, and the Wigner $\mathcal{D}$-matrix (see Appendix 6.3).

In any case, since we are only interested in E_0^k in the lab frame, we will only look at an expression for it. Following the results in Appendix 6.3, we find

$$[E_0^k]_{\mathrm{lab}} = \mathcal{D}(\mathbf{R})E_0^k\mathcal{D}^\dagger(\mathbf{R}) = \sum_{q'=-k}^{k} E_{q'}^k \mathcal{D}_{0q'}^k(\mathbf{R}).$$

Since the excitation pulse is linearly polarized, we only worry about the $q' = 0$ term in the sum. So, from our results in Appendix 6.3,

$$[E_0^k]_{\mathrm{lab}} = E_0^k \mathcal{D}_{00}^k(\mathbf{R}(0, \theta, \phi)) = E_0^k P_k(\cos\theta).$$

Dropping the subscript $[\cdot]_{\mathrm{lab}}$, we have an expression for the amount of light polarized, up to some extra factors:

$$E_0^k U_0^k = (2k+1)\begin{pmatrix} 1 & 1 & k \\ 0 & 0 & 0 \end{pmatrix}^2 P_k(\cos\theta).$$

Notice that this term vanishes when $k = 1$. So, we only have $k = 0, 2$ and conclude that

1. The **population** terms ($k = 0$) are angle-independent. ($P_0(\cos\theta) = 1$.)

2. No **orientation** ($k = 1$) can be induced or detected using linear polarizers.

3. The angular dependence for the **alignment** ($k = 2$) is $3\cos^2\theta - 1$, which means there exists an angles between the two polarizers ($\theta = 54.7° \equiv \theta_m$) for which no alignment effects will be observed. θ_m is referred to as the *magic angle*.

3 Experiment

3.1 Experimental overview

The goal of this work is to measure the lifetimes of the $5p_{1/2}$ and $5p_{3/2}$ states in potassium-39. To this end, we excite a sample of potassium-39 atoms in a magneto-optical trap (MOT) with a short pulse of 405 nm laser and record the decay fluorescence $5p_{1/2}, 5p_{3/2} \rightarrow 4s_{1/2}$ as a function of time. An overview of this experiment is given in Figure 5. For a comprehensive description of our MOT, the reader may refer to [19].
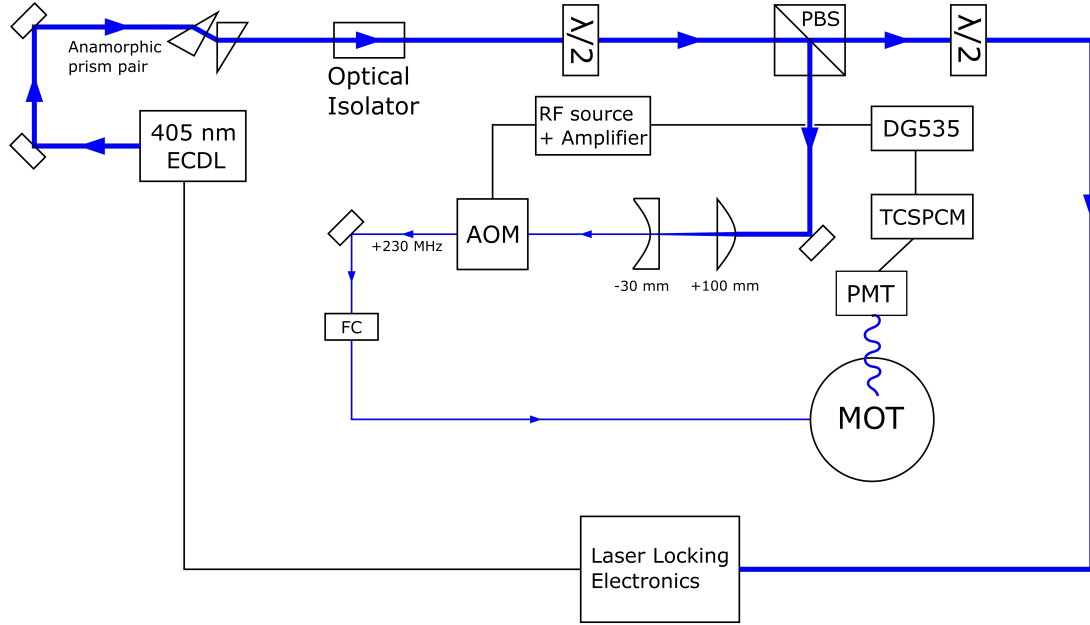
Figure 5: Optical arrangement for the tunable 405 nm ECDL used to drive the $4p_{1/2}, F = \{1, 2\} \rightarrow 5p_{1,2}, 5p_{3/2}$ transitions and electronics for the experiment.

The 405 nm laser used in this experiment is an external-cavity diode laser (ECDL). An adjustable diffraction grating allows for tuning the laser wavelength to excite either the $5p_{1/2} \leftrightarrow 4s_{1/2}$ or $5p_{3/2} \leftrightarrow 4s_{1/2}$ transition. As shown in Figure 5, the 405 nm laser is frequency-stabilized via Doppler-free saturated absorption spectroscopy, ensuring stable operation of up to several hours. The 405 nm laser is locked to the crossover point, so that a frequency shift of $\pm$ 230 MHz due to the acoustic-optic modulator (AOM) allows us to select to either excite from the $4s_{1/2}, F = 1$ or $4s_{1/2}, F = 2$ to the 5p states. The

wavelength corresponding to each transition is shown in Figure 6, which also shows the $4s_{1/2} \leftrightarrow 4p_{3/2}$ transition used for trapping. During the course of the lifetime measurement, the 770 nm trap beams remain in continuous operation. While this introduces (a small) ac-Stark splittings in the $4s_{1/2}$ and $4p_{3/2}$ state, the effect does not impact the fluorescence profile or the resulting lifetime.
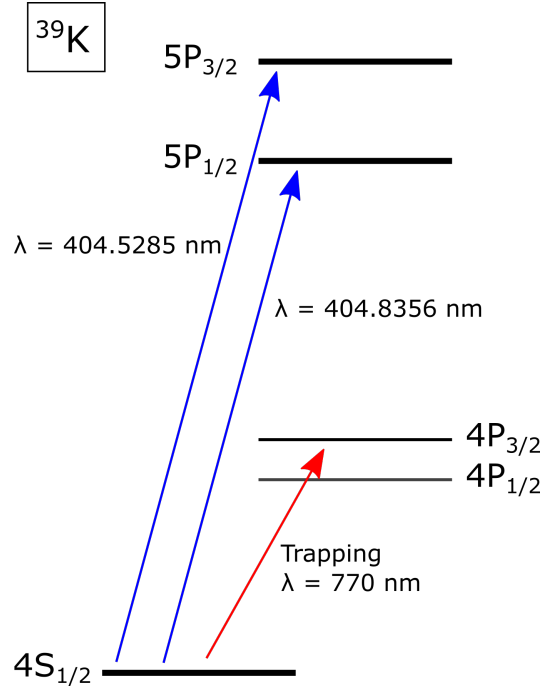
Figure 6: $4s_{1/2}$, $5p_{1/2}$, and $5p_{3/2}$ energy levels in potassium-39.

As is often the case with diode lasers, the beam directly out of the 405 nm ECDL is elliptical and thus requires passing through an anamorphic prism pair to obtain a more circular profile. The light then passes through an optical isolator to prevent reflection of the beam from other optical components back into the laser diode cavity. A combination of a half-wave plate and a polarizing beamsplitter regulate and direct the 405 nm light to two branches. On one branch, the light is sent to a vapor cell for frequency-stabilizing the ECDL. On the other, the beam is reduced in size and collimated by a factor of approximately 3.3 by a telescope comprised of a Thorlabs plano-convex lens with $f_1 = 100$ mm and a Thorlabs plano-concave lens with $f_2 = -30$ mm. This optical system enables

fast switching by the AOM (whose speed is limited by the beam diameter). The rise/fall time of the modulation is approximately 40 ns, which is sufficiently fast for the expected lifetimes ($\approx$ 30% of $\tau_{5p_{1/2}}$, $\tau_{5p_{3/2}}$)). Without this optical arrangement, the switching time is about 80-100 ns. The ability to produce and switch short pulses is crucial in our lifetime measurement, since it allows for generating broadband excitation pulses to resolve quantum beats and reduce systematic errors in analyzing the decay profile. With a modulation efficiency of 25%, our AOM allows us to send via a polarization-maintaining single-mode optical fiber (with $\sim$ 40-50% efficiency) roughly 0.4 mW of the 405 nm light to the MOT cloud. Since the trap lasers cause a majority of the atoms in the MOT to be in the $4s_{1/2}$, $F = 1$ state at any given time, we select the up-shifted beam (+230 MHz) from the AOM output to drive the $4s_{1/2}$, $F = 1$ to $5p_{x/2}$ transitions. By selection rules, exciting from the $F = 1$ sublevel of the ground state $4s_{1/2}$ with a sufficiently broadband 405 nm source lets us reach both the $F = \{1, 2\}$ sublevels of the $5p_{1/2}$ and the $F = \{0, 1, 2\}$ sublevels of the $5p_{3/2}$. A detailed but not-to-scale energy diagram for these hyperfine levels is shown in Figure 7. In the absence of magnetic fields, Section 2 tells us that only coherent excitation of the hyperfine-level manifold $F = \{0, 1, 2\}$ of the $5p_{3/2}$ state can result in quantum beats in the decay profile.

The light exiting the AOM is coupled to a polarization-maintaining fiber and sent through the MOT as shown in Figure 8. The MOT cloud is approximately 1 mm in diameter, with number density 10^8-10^9 atoms/cm^3. The MOT coils generate a magnetic field gradient of 1 G/mm. The vacuum chamber containing the MOT is equipped with shim coils, which allow us to adjust the position of the MOT cloud inside the vacuum chamber. Based on previous experiments, we expect the center of the MOT cloud to experience a magnetic field strength of 0.3-0.5 G. This variation in magnetic field strength across the MOT cloud is expected to result in Zeeman beats whose frequencies are on the order of the lifetimes of $5p_{1/2}$ and $5p_{3/2}$ states.

Due to various physical constraints, the 405 nm beam and the optical components for fluorescence detection, which must be perpendicular to the k-vector of the excitation beam,
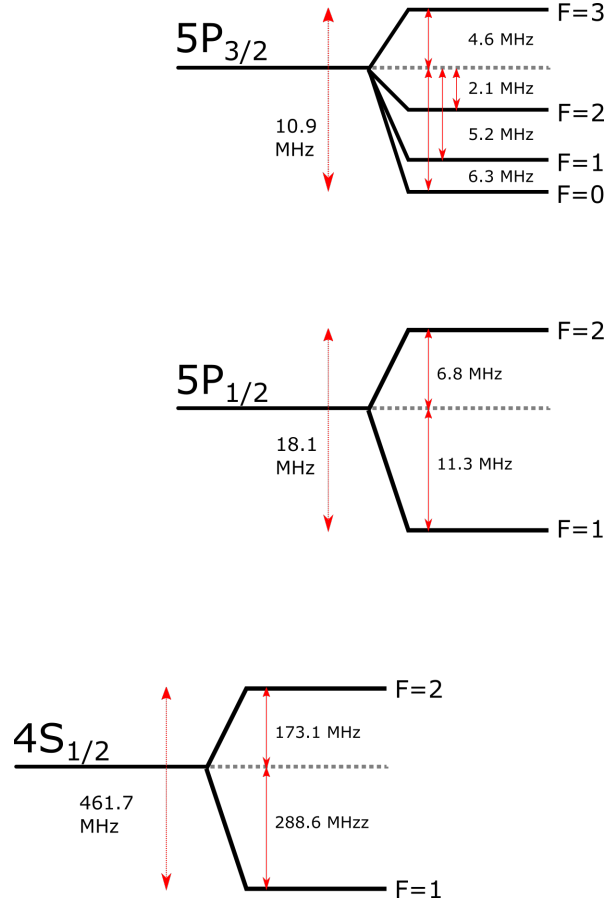
Figure 7: Hyperfine energy levels of the $4s_{1/2}$, $5p_{1/2}$, and $5p_{3/2}$ states in potassium-39, from [11] and [12].

are off-axis with respect to the MOT beams, as illustrated in Figure 9. The detection system consists of linear polarizer making an angle θ relative to the (linear) polarization of the 405 nm beam, followed by a 405 nm bandpass filter and a plano-convex lens with $f_3 = +50$ mm for imaging the MOT cloud (which has a diameter of ~ 1 mm) at a distance of 12 cm onto an optical fiber tip with a diameter of roughly 100 μm. The linear polarizer has a transmission efficiency of roughly 70% at 405 nm.

The Hamamatsu PMT has quantum efficiency of roughly 30% at 405 nm. The fiber transmits the collected fluorescence to the PMT, which is connected to the TimeHarp 260 time-correlated single-photon counting module (TCSPCM) for data acquisition. The Time-
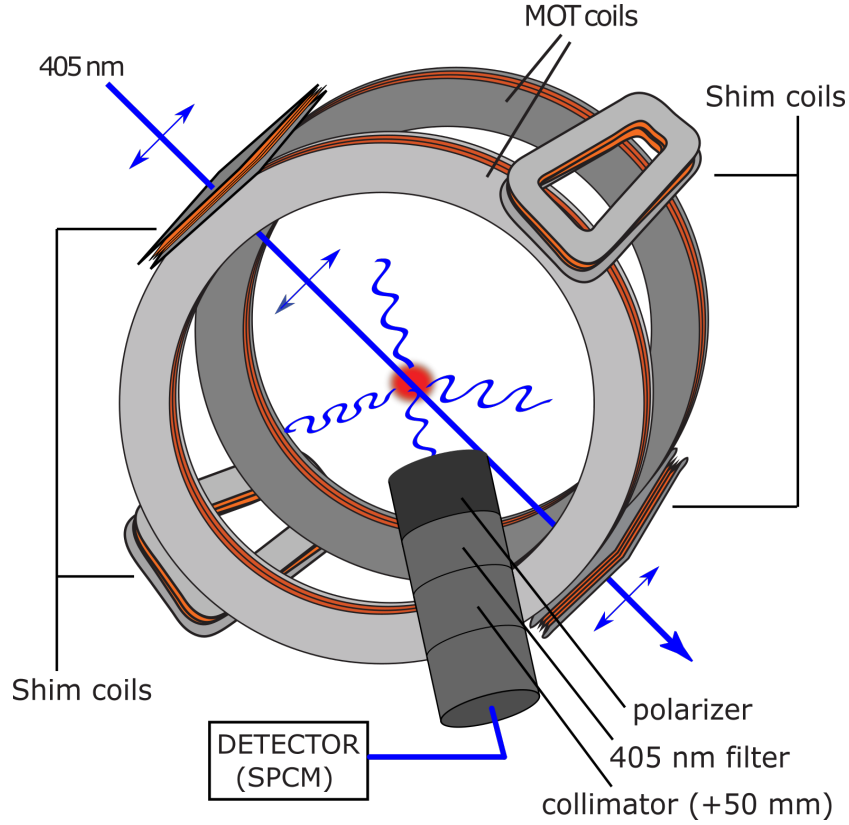
Figure 8: The MOT-based excitation and detection scheme.

Harp 260 can acquire data with a maximum timing resolution of 0.25 ns per bin. However, in all of our experiments, we take data at 2 ns per bin (approximately 1% of the lifetimes in consideration), to achieve higher counts per bin. Other capabilities of the TimeHarp 260 can be found on its data sheet, which is available for download on PicoQuant's website [20]. In Section 4.1.1, we will discuss its timing uncertainty, differential non-linearity, among other limitations, and how they could contribute to the uncertainty of our measurement.

A single pulse generator DG535 is used to control the entire experimental timing sequence. The repetition rate is set to 250 kHz; this corresponds to a duty cycle of 4 µs. At time $T = 0$, the DG535 sends out a 230 MHz RF pulse AB of width t_{AB} to an amplifier. This signal then gets amplified and subsequently sent to the AOM, setting the width of the 405 nm pulse to t_{AB}. The typical range of t_{AB} is 70 ns to 1 µs. 1.25 µs after T, the DG535

also sends out a pulse CD with t_{CD} = 100 ns, which triggers the TimeHarp 260 to start the acquisition. The TimeHarp260 has to be triggered 1.25 μs *after* the pulse-switching trigger signal due mainly to the speed of sound inside the AOM crystal; if the TimeHarp 260 and AOM are triggered simultaneously, the TimeHarp260 will be recording data for roughly 1.25 μs before the acoustic wave inside the AOM crystal deflects the 405 nm beam into the MOT, and no fluorescence signal will be detected.
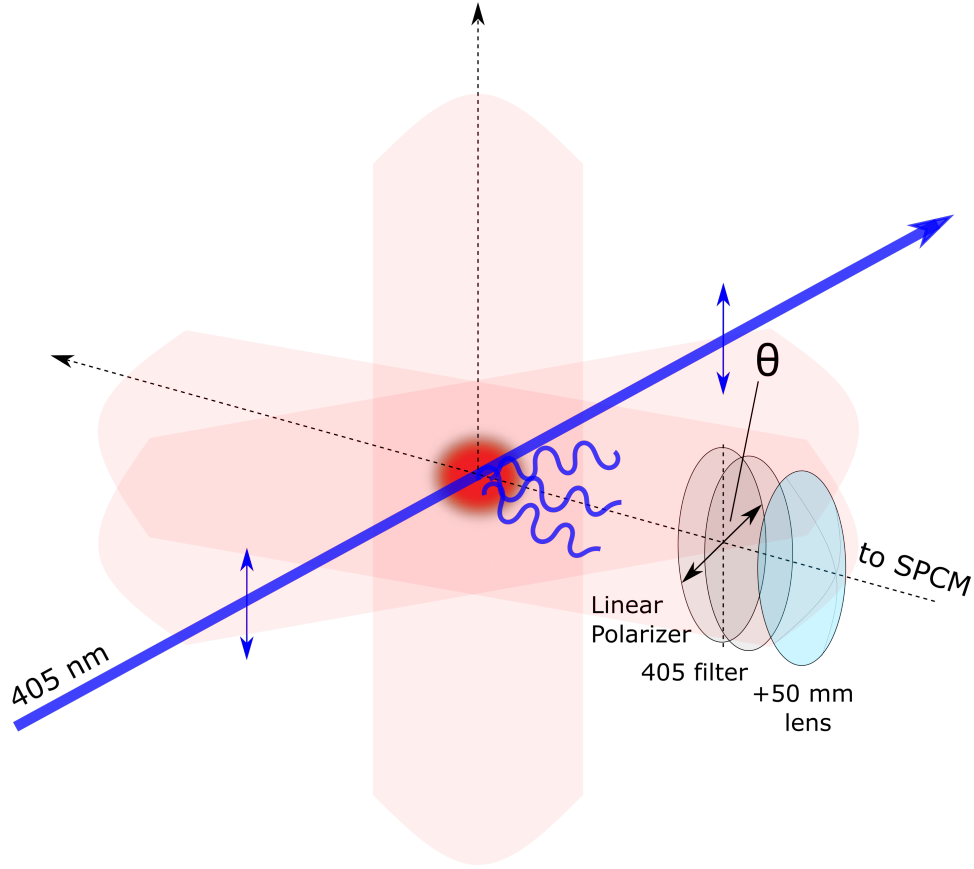
Figure 9: Excitation-detection geometry. The k-vector of the 405 nm beam is perpendicular to the axis of the detection system. The linear polarizer on the detection system makes an (adjustable) angle θ with the linear polarization of the 405 nm beam, which is fixed.

3.2 Review of previous measurements

3.2.1 The 5p$_{1/2}$ measurement

The measurement of the 5p$_{1/2}$ lifetime is rather straightforward since there are no quantum beats present in the decay profile, even with small magnetic fields as [1] and this work will show. Here, we review two previous measurements of $\tau_{5\mathrm{p}_{1/2}}$ by Berends [2] and Mills et al. [1]. The reader may refer back to Table 1 for the timeline of this measurement.

In [2], the lifetimes of the fine-structure components of the 5p, 6p, and 7p states in potassium-39 were determined using techniques of laser-induced fluorescence. Potassium vapor in a Pyrex cell was irradiated with broadband pulses of dye laser light which selectively excited each fine-structure state. The fluorescence resulting from the decay to the 4s ground state was monitored at right angles to the direction of excitation and registered with a monochromator and photomultiplier whose signal was amplified and analyzed with a transient digitizer interfaced to a computer, which produced a time-evolution histogram of the fluorescence. The glass cell was temperature-controlled and placed at the center of Helmholtz coils whose purpose was to eliminate Zeeman quantum beats (to $\pm\, 2\times 10^{-3}$ G) from the fluorescence decay spectrum. To completely remove hyperfine quantum beats, a linear polarizer was placed between the cell and the monochromator at the magic angle relative to the polarization axis. However, since the polarizer significantly reduced the signal-to-noise ratio, the polarizer was removed, and the Helmholtz coils were used to produce a magnetic field of 25 G in the cell. This shifted the frequency of quantum beats due to Zeeman effects (about 5 MHz) beyond the detection range of the transient digitizer, but still kept the Zeeman splitting small enough to ensure broadband excitation of the fine-structure state. This method gave higher signal-to-noise ratio and was the technique ultimately used by [2]. The report lifetime of the 5p$_{1/2}$ state was 137 ± 2 ns at temperature $T = 372$ K.

The approach used in [1] is more similar to this work's in the sense that the sample is a cloud of 3×10^6-3×10^7 potassium-39 atoms trapped in a MOT. Rather than collecting the

fluorescence as in [2], Mills et al. monitored the state population by pulsed excitation followed by nonresonant photoionization. The pulsed excitation is a frequency-stabilized (by Doppler-free saturation absorption spectroscopy) 405 nm diode laser drives the $4s_{1/2}, F = 1$ to $5p_{1/2}, F = 2$ transition. The photoionization beam, which co-propagates with the 405 nm beam and is left on at all times, is 763 nm laser light, which has enough energy to ionize the 5p state but not the lower-lying states but also sufficiently low power to prevent two-photon ionization from lower-lying states. For each 5 μs cycle, the MOT 766.5 nm beams are turned on to confine the atoms and then turned off. Roughly 100 ns after the 405 nm beam is completely off, photoions are counted for the remainder of the cycle. An electric field accelerates the ions towards a micro-channel plate detector, and measure the resulting count rate as a function of time. This work reports $\tau_{5p_{1/2}} = 137.6 \pm 1.3$ ns. Mills also reported that they observed no measurable quantum beats due to Zeeman effects.

3.2.2 The 5p$_{3/2}$ measurement

There are, in general, two approaches to measuring the lifetime of the 5p$_{3/2}$ state in the literature. One approach was presented in Berends et al. [2] using pulsed excitation and fluorescence detection, as discussed in the preceding subsection. On the other hand, the level-crossing technique was used in [4], [5], and [6] by Svanberg et al., Ney, and Schmieder et al. Roughly speaking, level-crossing technique which uses the spatial interference in the scattering of resonance radiation that can occurs when a Zeeman level of one of the hyperfine structure levels is brought into coincidence (which explains the terminology "crossed") with a Zeeman level of a neighboring hyperfine structure level by the application of an external magnetic field. The light spectrum must be board enough to excite all states in the manifold equally. From these experiments, one can extract the coefficients A_{hfs} and B_{hfs} as well as the lifetime τ by fitting a theoretical curve (which comes from the Breit-Wigner formula) to the curve of scattered light intensity as a function of magnetic field. When the signal resolution is low, which is typical of experiments of this kind, the *derivative* of the scatter intensity curve can be studied since it enhances the features of the original curve. This is the approach used in [4], [5], and [6]; however, significantly different results were reported (see Table 2). Only the more recent measurements by [2] and [4] ap-

pear to have better agreement. It is clear that more measurements are necessary to resolve this discrepancy in the literature.

4 Results and Discussion

4.1 The 5p$_{1/2}$ measurement

In this subsection, we report the measurement of $\tau_{5p_{1/2}}$. Our approach is as follows. While we did not expect quantum beats due to the hyperfine structure of 5p$_{1/2}$ to occur, we still tested for quantum beats by driving the $4s_{1/2} \rightarrow 5p_{1/2}$ with short pulses (60-70 ns) to coherently excite both the $F = 1$ and $F = 2$ hyperfine levels and set the angle θ between the excitation and detection vectors at 0 and 90 degrees. Figure 10 shows one data set from this test. It is clear that were no detectable quantum beats. We also ran similar experiments without the polarizer on the detector at different pulse widths (see Figures 11 and 12), and observed the same decay profile with no oscillations in time. As a result, we concluded that there were no quantum beats due to magnetic effects. This allowed us to remove the polarizer on the detector to increase our signal-to-noise ratio (by a factor of approximately 2) and use a longer pulse to excite more atoms into the 5p$_{1/2}$ state. In the rest of the experiments for the 5p$_{1/2}$ measurement, we held this configuration and considered systematic errors. These include errors due to the electronics (time calibration, pulse pile-up, etc.) and radiation trapping. Once all the systematic errors were accounted for, we took the average of our measurements and combined it with the estimated uncertainty to obtain our final result (see Table 3). We note that unlike in [1] where photoionizaton was used to record the decay profile, our approach (fluorescence detection) does not require an estimate for uncertainties due to quantum beats.

4.1.1 Systematic Errors

Timing uncertainty and Differential nonlinearity in time-to-digital converter. The timing uncertainty from the trigger, according to the TimeHarp 260 data sheet, is 250 ps + $10^{-8}\Delta t$ where Δt is how long after the trigger that the pulse comes in. Here, $\Delta t \approx 10^6$ s, so the time uncertainty is effective 250 ps. We thus see that this uncertainty is negligibly small and can be combined with the uncertainty due to the nonlinearity between the channels (i.e., that, giving a uniform light source, some channels might systematically acquire more counts than others). According to the data sheet of the TimeHarp 260, the differential non-

Source of error	Value
Timing uncertainty + Nonlinearity	$\pm\, 0.1\%$
Truncation uncertainty	$\pm\, 0.4\%$
Pulse pile-up correction	$-\, 0.1\%$
Radiation trapping	$\pm\, 0.2\%$
Other statistical errors	$\pm\, 0.2\%$
Result	**138.8 ± 1.6 ns**

Table 3: List of systematic and statistical errors and how they were estimated. The errors shown are from independent physical processes and so are added in quadrature.

linearity is less than 0.2% rms. This means that, given a uniform light source, the standard deviation in the counts across all bins is within 0.2% of the mean count. Equivalently, we can think of the the 0.2% rms as the fractional standard deviation in the bin size, which in our case is 0.2% of 2 ns. The data sheet also specifies a 2% peak-to-peak nonlinearity. To convert this nonlinearity into an uncertainty in our measurement, we produced a pure exponential plus Gaussian noise to represent the nonlinearity. In IGOR, we create a histogram with bin size of 2 ns per bin for a pure exponential $Ae^{-t/100}$ multiplied by Gaussian noise, plus background noise. Our simulation leads to an estimate of $\pm\, 0.1\%$ uncertainty in the lifetime.

Pulse pile-up. The pulse pile-up effect occurs when photons are lost at high photon count rates due to the dead time of the detector and/or electronic counting module. The dead time of a device the time the device needs to process the detected photon and get ready for the next. If the repetition rate or count rate is too high compared to the dead time of the device, the photon loss creates two undesirable effects:

- The measured lifetimes become shorter

- A single exponential decay may becomes double exponential with an additional

Figure 10: No quantum beats observed in the decay from the $5p_{1/2}$ state. The excitation pulse width is 70 ns. The relative angle between the detection and excitation polarization vectors is 90 degrees. An exponential (black) was fitted to the data, giving a lifetime of approximately 138.6 ns with a fit uncertainty of 0.2 ns. The normalized fit residual shows no resolvable quantum beats.

shorter component.

Pulse pile-up can distort histograms and render parts of the data poor for fitting. While it is possible to correct for pulse pile-up using the following formula, due to [21]

$$N_i' = \frac{N_i}{1 - \frac{1}{N_E} \sum_{j<i} N_j}$$

where N_E is the number of excitation cycles, N_i is the observed number of counts in channel i, and N_i' is the true number of counts in the ith channel, in practice it is best to avoid having a count rate that is comparable to the repetition rate. In our experiment, the dead time of the TimeHarp 260 is 2 ns, the dead time of the Hamamatsu PMT is 18 ns, the repetition rate is between 200-250 kHz, and the typical count-rate is approximately 1-2 kHz. Since the count rate is much less (only approximately 1%) of the repetition rate, the
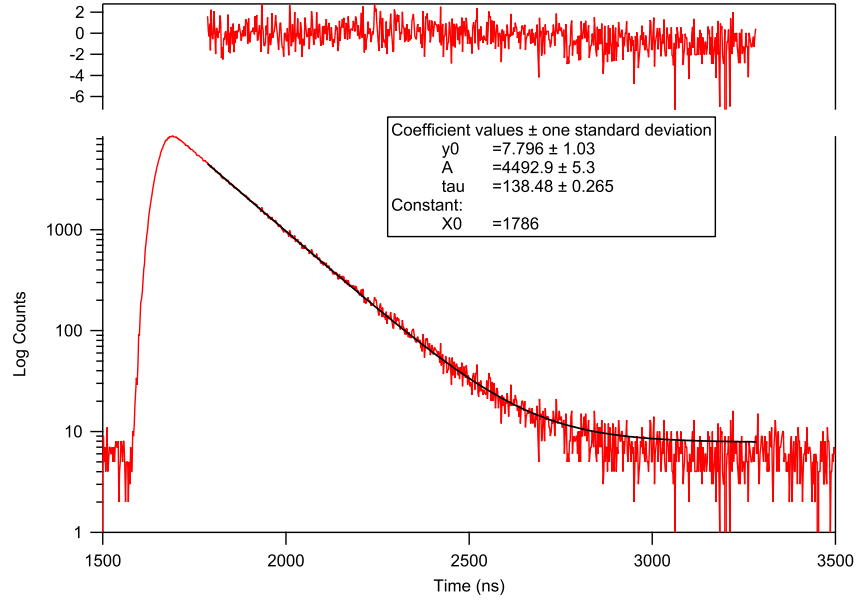
Figure 11: No quantum beats observed in the decay (red) from the $5p_{1/2}$ state. The excitation pulse width is 70 ns. The detector had no polarizer attached. An exponential (black) was fitted to the data, giving a fitted lifetime of approximately 137.8 ns with a fit uncertainty of 0.2 ns. The normalized fit residual shows no resolvable quantum beats.

correction due to pulse-pile up is small. To see this, we consider the following back-of-the-envelope calculation. For a typical experiment, we take data for about 10 minutes. This gives $N_E \approx 10^8$, while $\sum_{j<i} N_j$ is at most 2×10^6. As a result, the denominator in the correction formula above is at least 0.97. However, this calculation assumes that the pulse-pile up at bin i comes from all bins $j < i$. In reality, this is not the case due to the small dead time of our detector (≈ 20 ns), which removes the need to sum over all $j < i$ channels. At 20 ns dead time and 2 ns per bin resolution, we only sum over 10 bins. The denominator, in this case, is approximately 0.997-0.998 at most, and the pulse pile-up is even smaller. Applying this correction to our data, we find a correction of at most 0.1% to the counts per bin, which happens at high-count bins. Re-fitting the corrected data, we find that the variation in the fitted lifetime there is a correction of roughly -0.1% to the lifetime. We choose to call this a $\pm 0.1\%$ uncertainty in the lifetime rather than refit.
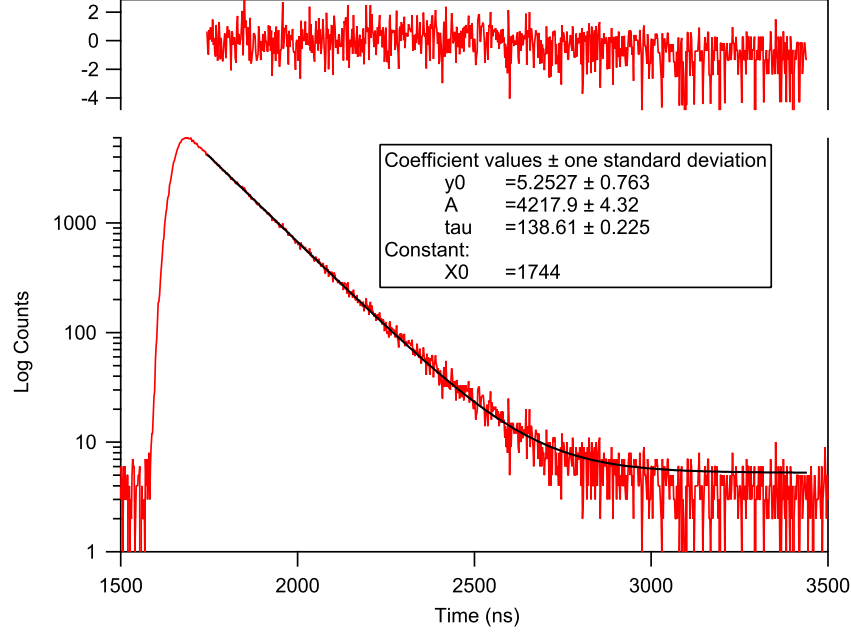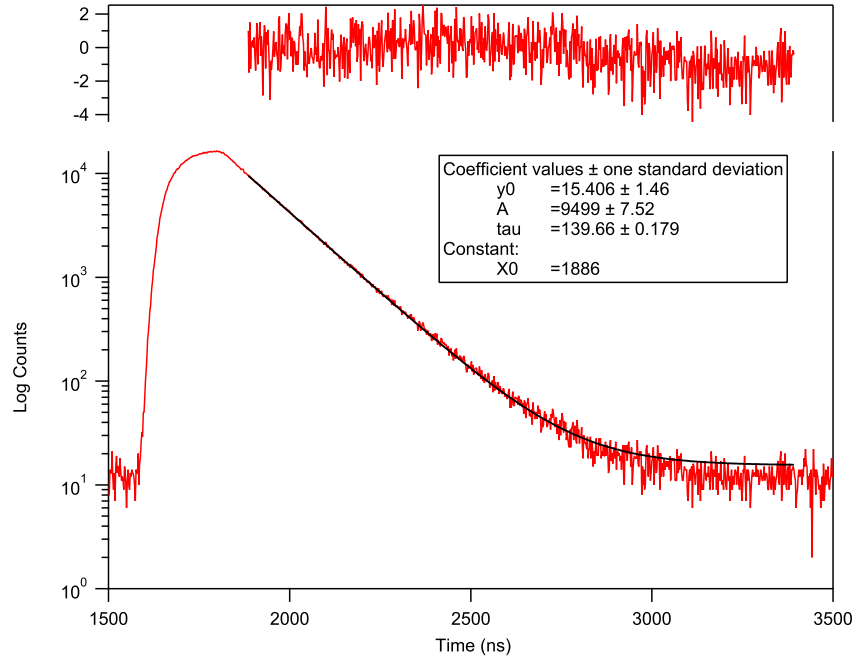
Figure 12: No quantum beats observed in the decay (red) from the $5p_{1/2}$ state. The excitation pulse width is 200 ns. The detector had no polarizer attached. An exponential (black) was fitted to the data, giving a fitted lifetime of approximately 138.5 ns with a fit uncertainty of 0.1 ns. The normalized fit residual shows no resolvable quantum beats.

Truncation uncertainty. There is a variation in the lifetime for fits over different ranges of the data. We typically begin our fit at 80-90% the falling edge and end when the signal has sufficiently decayed. To quantify uncertainty due to data truncation when fitting, we select one set of data and perform fits for various start and ends points. As expected, the fitted lifetimes vary over these fits. We then calculate the (fractional) standard deviation in the fitted lifetimes. We then repeated the process for a few additional datasets and found that an uncertainty of roughly $\pm\,0.4\%$ accounts for the variation in the lifetimes from the truncation when fitting. It turns out that the truncation error is the dominant source of uncertainty in our measurement of $\tau_{5p_{1/2}}$.

41
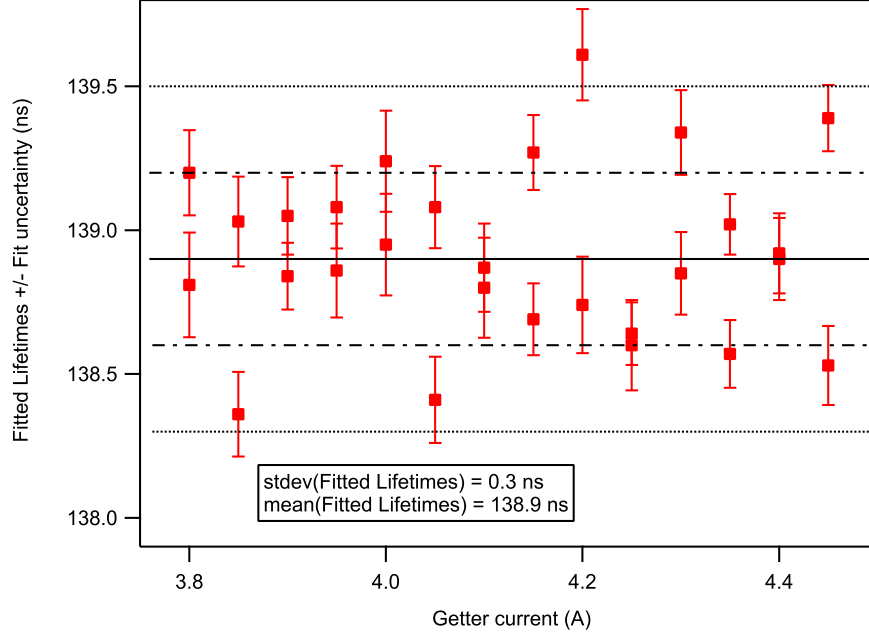
Figure 13: Fitted lifetimes (ns), with fit uncertainties, versus the getter current (A), which controls the density of the MOT cloud. The plot shows no significant trend in the lifetime.

Radiation trapping. Radiation trapping comes from the re-absorption of the emitted photon by the sample itself. This effect depends on the length and density of the sample and could increase the measured lifetime substantially when there are many atoms. Since the MOT has small size, radiation trapping is a much smaller effect here than in an experiment with a vapor cell. If we denote the length and density of the sample as l and n and the atomic absorption coefficient as α, the change in the measured lifetime due to this effect is given by [22]:

$$\frac{\tau'}{\tau} = 1 + \left(\frac{C}{\lambda}\right)^2$$

where

$$C = l\alpha n = \lambda \tan(\lambda),$$

where

$$\alpha = \frac{\lambda^3}{2\pi} \frac{\Gamma_{5p\to4s}}{\Gamma_{\text{total}}} \approx 4 \times 10^{-11}\,\text{cm}^2$$

42

In the limit of small length, this equation becomes

$$\tau' - \tau = \tau C = \tau l \alpha n,$$

where the change of lifetime depends linearly on density. With path length $l \approx 0.5$ mm and density $n \approx 10^9$ cm^{-3}, we estimate a correction of $(\tau' - \tau)/\tau \approx 0.2\%$ to the lifetime.

To test for radiation trapping experimentally, we looked for trends in the measured lifetime as a function of the getter current, which controls the density of our sample. Figure 13 shows no detectable trend in lifetime above statistical variations between measurements. We conclude that the error due to this effect is approximately $\pm$ 0.2%, which is roughly the size of the fit uncertainty and is consistent with we estimate in the preceding paragraph.

4.1.2 Statistical Errors

We let the computer-generated fit uncertainty be the statistical error in our measurement. A typical fit uncertainty is approximately $\pm$ 0.3 ns, which corresponds to about $\pm$ 0.2% of the lifetime.

4.2 The 5p$_{3/2}$ measurement

The presence of quantum beats in the 5p$_{3/2}$ decay makes the measurement much more technically challenging. As discussed in the preceding sections, there are two sources of quantum beats: the hyperfine structure of the 5p$_{3/2}$ state, and Zeeman splittings within the hyperfine sublevels. In order to create and observe quantum beats, we first excite the atom cloud with a 70 ns pulse of linearly-polarized 405 nm light to coherently excite the ground state 4s$_{1/2}$ $F = 1$ to the 5p$_{3/2}$, $F = \{0, 1, 2\}$ manifold, then detect the fluorescence through a linear polarizer making an angle θ with the excitation polarization. Figure 14 shows the observed quantum beats for various values of θ. We note that it is possible to excite from the F = 2 hyperfine state to the 5p$_{3/2}$ F states and still observe higher-frequency quantum beats. However, even though we could find quantum beats, the signal-to-noise ratio was poorer than the excitation from the 4s$_{1/2}$ F = 1 due to the trap repumping mechanism.
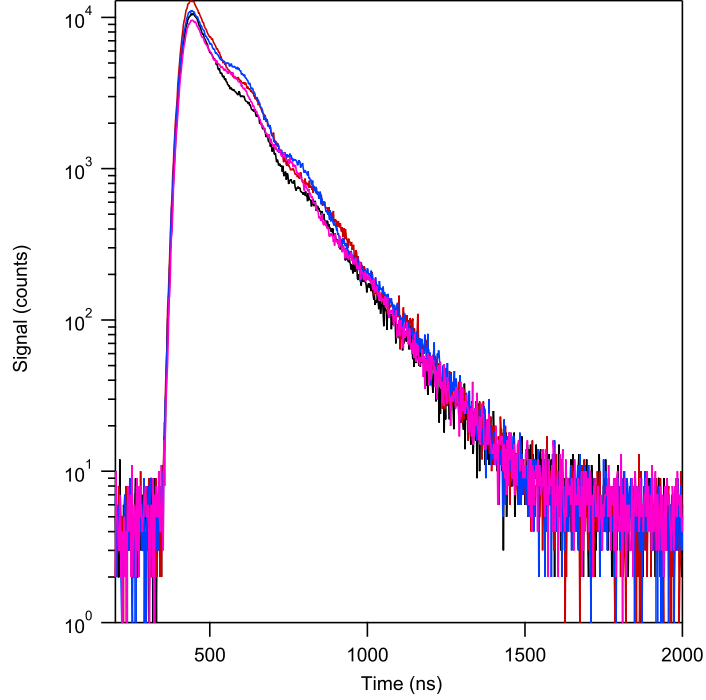
Figure 14: Observed quantum beats in the $5p_{3/2}$ decay fluorescence for various values of θ. The quantum beats are due to the spacings between hyperfine sublevels in the $5p_{3/2}$ state as well as Zeeman effects.

In order to reliably extract the (dominant) oscillation frequency within the decay profile, we fit this decay curve with the following theoretical curve of the form

$$f(t) = Ae^{-t/\tau}(1 + B\cos(\omega t + \varphi)), \tag{10}$$

where A, B represent the amplitudes of the decay curve and the fraction of the oscillation, respectively, ω is the dominant oscillation frequency, φ is the phase, and τ is the lifetime. While it is theoretically possible to fit this curve to the decay profile and extract both the beat frequency and lifetime of $5p_{3/2}$, in practice we find that due to the uncertainty in the phase of the oscillation, the fitted lifetime can be highly unstable, varying up to a few ns across various fit-start and end points (This is further confounded by truncation error). The fitted oscillation frequency, however, is more stable and is approximately 5-6 MHz. While this is on the same order of magnitude as the hyperfine splittings between the F states of $5p_{3/2}$, this value for the beat frequency does not agree with the splittings, which

suggests that magnetic effects are present.

To completely eliminate quantum beats using the magic-angle setup, there must be zero magnetic field in the region of space which the atom cloud occupies. This is not possible to achieve in a MOT setup, since the MOT cloud has finite size and requires a non-zero magnetic field gradient to form. As pointed out in the 3.1, the MOT cloud has diameter of 1 mm, the magnetic field gradient is 1 G/mm, and the center of the MOT cloud may experience a magnetic field strength of about 0.3-0.5 G. As a result, by narrowly focusing the 405 nm beam and setting the excitation-detection relative polarization angle to the magic angle $\theta_m = 54.7°$, it is possible selectively excite different regions within the MOT cloud and find where the quantum beats are minimized. Figures 15, 16, and 17, show how the amplitudes of quantum beats change as different portions of the MOT cloud is excited. In Figures 15 and 16, the beat amplitudes are large. By adjusting the aim of the 405 nm laser to excite a different portion of the cloud in lower magnetic field, we can reduce the beat amplitudes, as evident in Figure 17. The fit (10) performs quite well for the small-beat case, as there are no oscillations in the normalized residual. The fit is quite poor for the case where the quantum beat amplitudes are large – there are clear oscillations in the normalized residuals in Figures 15 and 16.

With this method, we find that the lifetime of the $5p_{3/2}$ state is approximately 136.0 $\pm$ 2.4 ns. Here, we assume that the systematic errors and their values are the same before, except for the truncation error, which is much larger now because the fitted lifetime is highly dependent on the starting location of the fit (even though we have the "phase" parameter in our fit function). We see fitted lifetimes as small as roughly 134 ns, which is the value obtained experimentally by [4] and [2] and theoretically by [3], to as high as $\sim$ 140 ns, which is what [6] found. The error budget and the value for the lifetime of $5p_{3/2}$ using the short-pulse approach are given in Table 4.

There are a number of possible solutions to this quantum beats problem in our MOT-based approach. The most natural solution is to switch off the magnetic fields before

Figure 15: Large quantum beat amplitudes in the $5p_{3/2}$ when a portion of the MOT cloud in high magnetic field is excited. The fit function (10) performs quite poorly, as evident in the oscillations in the normalized residuals.

[Short pulse] Source of error	Value
Timing uncertainty + Nonlinearity	$\pm\,0.1\%$
Truncation uncertainty	$\pm\,1.8\%$
Pulse pile-up correction	$-\,0.1\%$
Radiation trapping	$\pm\,0.2\%$
Other statistical errors	$\pm\,0.2\%$
Result (short-pulse approach)	$\mathbf{136.0 \pm 2.4\ ns}$

Table 4: List of systematic and statistical errors, their values, and the value for $\tau_{5p_{3/2}}$ using the short-pulse approach. The errors are added in quadrature. Again, the dominant error is truncation error, but it is 4-5 times larger than that in the $\tau_{5p_{1/2}}$ measurement.
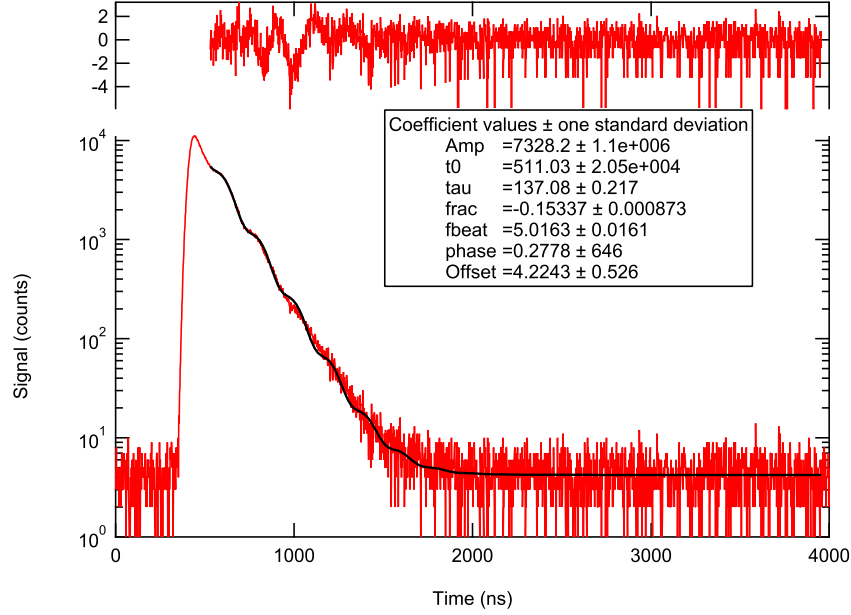
Figure 16: Large quantum beat amplitudes in the $5p_{3/2}$ when a portion of the MOT cloud in high magnetic field is excited. Quantum beats are slightly suppressed compared to Figure 15. However, the fit function (10) still performs quite poorly. Oscillations in the normalized residuals are still present.

driving the $4s_{1/2} \rightarrow 5p_{3/2}$ transition with the 405 nm pulses. However, this approach comes with a number of disadvantages of which the most significant is repetition rate. Due to the non-zero inductance of the metallic parts in the MOT chamber and the MOT Helmholtz coils, the magnetic field (gradient) takes roughly a few ms to sufficiently decay away. Within this time, the MOT cloud also expands and disintegrates. As a result, the count rate, even if the repetition rate is 250 kHz, would be much lower compared to having the magnetic field on continuously. Overall, we estimate that with the magnetic-field-switching approach, we will need to take data for at least 10 times longer to get the same statistics as we have with the current approach.

An alternative approach is to drive the $4s_{1/2} \rightarrow 5p_{3/2}$ transition using longer 405 nm pulses. The idea behind this approach is the following: by using the longer pulse, we expect that the quantum superpositions of the hyperfine sublevels will decohere, and so
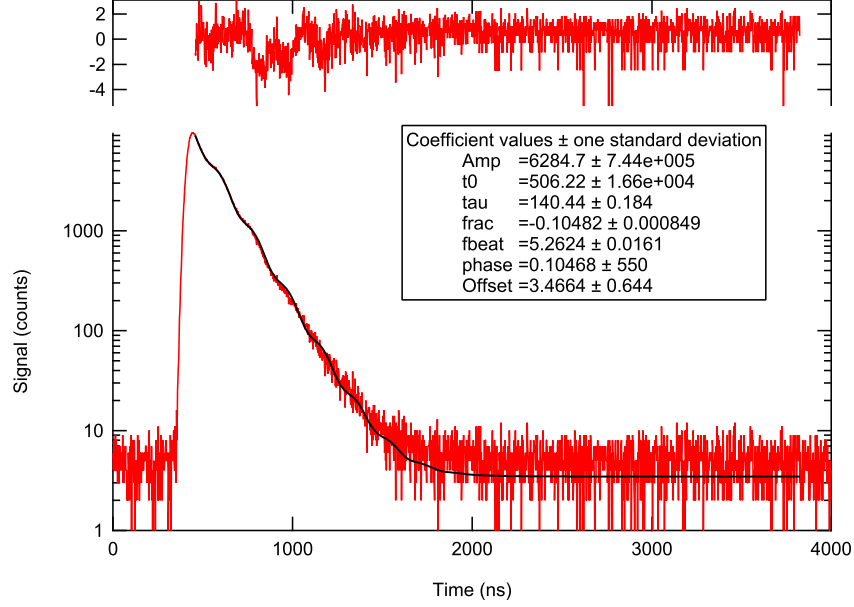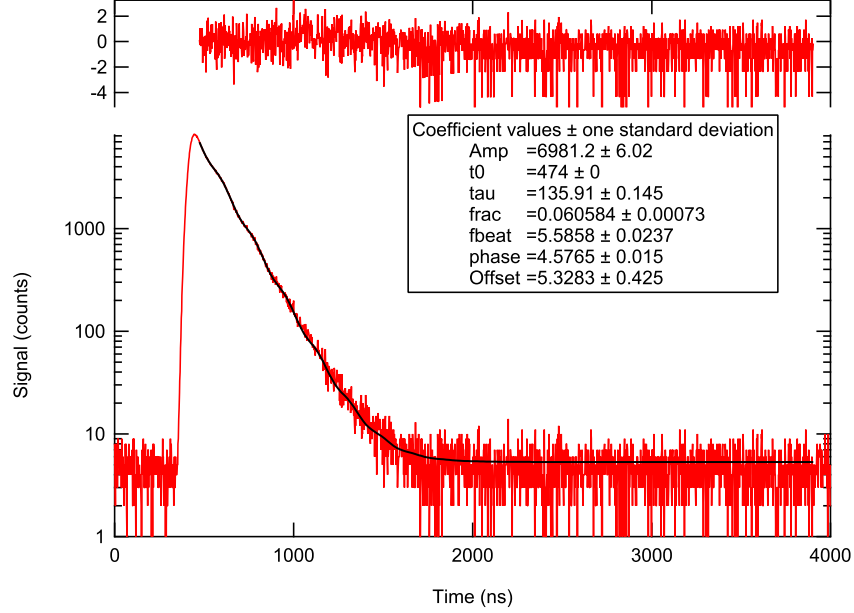
Figure 17: Smaller quantum beat amplitudes in the $5p_{3/2}$ when a portion of the MOT cloud in low magnetic field is excited. Quantum beats are largely suppressed. The oscillations in the normalized residual are minimal.

quantum beats will "average out," resulting in a beatless decay. One advantage of this approach is that we can remove the linear polarizer in front of the detector, since the spatially anisotropic fluorescence will also be averaged out. In our experiment, we used 1 μs instead of the 70 ns 405 nm pulses to excite to the $5p_{3/2}$ states.

Figures 18 and 19 show the decay profiles in these cases, fitted to the function in (10). We notice that even with a much longer pulse quantum beats are still present despite being quite minimal compared to using a short pulse (The beats can be seen most clearly in the normalized residuals in Figure 18). By exciting parts of the MOT cloud in low magnetic fields, these quantum beats can be further suppressed (see Figure 19). With this method, we find that the lifetime of the $5p_{3/2}$ state is approximately 137.6 ± 3.7 ns. Once again, we assume that all systematic/statistical errors are the same as before except for the truncation error. Table 5 gives the values for the error and $\tau_{5P_{3/2}}$ for the long-pulse approach. The only differences between 5 and 4 are the truncation error and the mean observed $\tau_{5P_{3/2}}$.

48
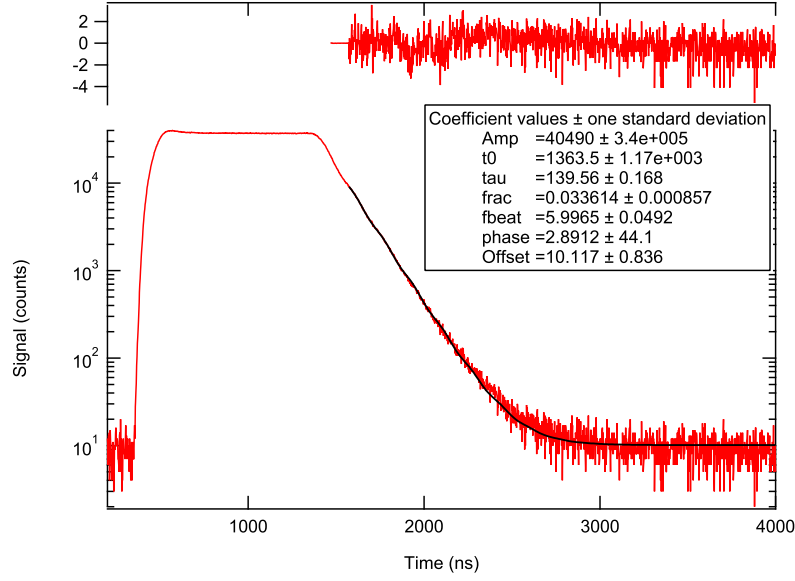
Figure 18: $5p_{3/2} \rightarrow 4s_{1/2}$ decay profile. Quantum beats are still present (as one can see in the normalized residual), even with a long excitation pulse. Using the fit function (10), we find a lifetime of approximately $\tau_{5P_{3/2}} \approx 139.6 \pm 0.2$ ns, where ± 0.2 ns is the fit uncertainty. The fractional amplitude of quantum beats is 0.03, which is not as big an improvement as we might expect, is possibly due to the short turn-off time of the 405 nm pulse.

[Long pulse] Source of error	Value
Timing uncertainty + Nonlinearity	$\pm 0.1\%$
Truncation uncertainty	$\pm 2.2\%$
Pulse pile-up correction	$- 0.1\%$
Radiation trapping	$\pm 0.2\%$
Other statistical errors	$\pm 0.2\%$
Result (long-pulse approach)	$\mathbf{137.6 \pm 3.1}$ **ns**

Table 5: List of systematic and statistical errors, their values, and the value for $\tau_{5P_{3/2}}$ using the long-pulse approach. The errors are added in quadrature.
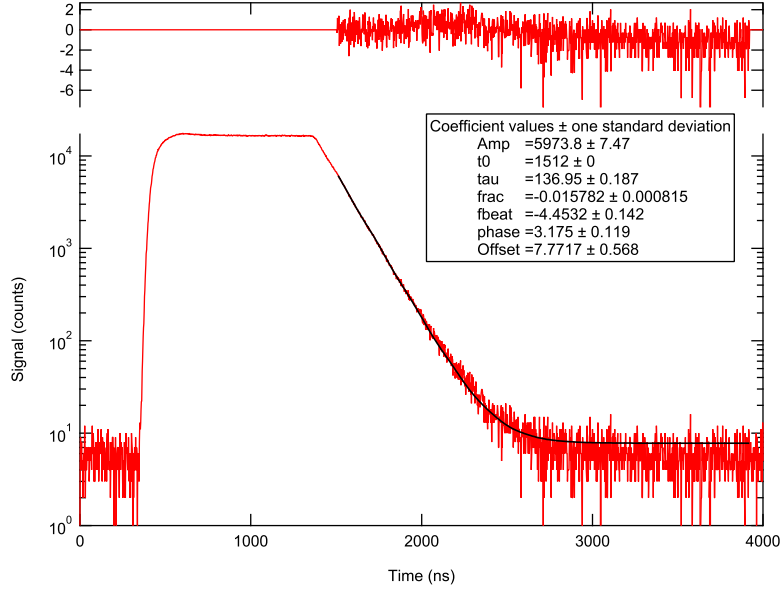
Figure 19: $5p_{3/2} \rightarrow 4s_{1/2}$ decay profile. By selecting a portion of the cloud in low magnetic fields, quantum beats can be suppressed further.

5 Conclusions

We measured the lifetimes of $5p_{1/2}$ and $5p_{3/2}$ of ^{39}K by exciting a cloud of ^{39}K atoms in a magneto-optical trap by a linearly-polarized pulse of 405 nm light followed polarization-specific, time-resolved fluorescence detection. We find $\tau_{5p_{1/2}} = 138.8 \pm 1.6$ ns, which is consistent with past measurements [1], [2] and calculations [3]. using two slightly different approaches, we obtained two measurements for the $5p_{3/2}$ lifetime: 137.6 ± 3.1 ns and 136.0 ± 2.4 ns, obtained from two slightly different approaches. These measurements are consistent with past measurements [2], [4], [5], [6] and theoretical calculations in [3]. It is clear that future work is needed to reduce the uncertainty in our measurement and resolve the discrepancy in the literature.

6 Appendix

6.1 Quantum beat theory in the density matrix formalism [8]

The density matrix formulation greatly simplifies many quantum-beat calculations. This is because the optical signals in a fluorescence experiment turn out to be proportional to the mean value of some atomic observable in the excited state e, which can be very easily expressed as a combination of components of the density matrix $\rho_e(t)$ of this state. The evolution of $\rho_e(t)$ due to the light excitation process, to the precession of the coherences in the atomic excited state and to spontaneous emission is adequately described by a set of linear differential equations, whose solution yields $\rho_e(t)$ and allows the explicit calculation of the atomic fluorescence signal as a function of time. Furthermore, the atomic density matrix $\rho_e(t)$ may be represented as an expansion over a set of spherical tensor operators among which only the scalar, dipolar and quadrupolar terms affect the fluorescence light.

Let us begin from the QED derivation of the quantum beat signal for a single-atom system. At $t = 0$, we assume that the system is prepared by the light pulse in the state

$$|\psi(0)\rangle = \sum_i \alpha_i |e_i, 0\rangle, \quad i = 1, 2,$$

where $|e_i, 0\rangle$ represents the atom in substate $|e_i\rangle$ with no photon present. α_i are of course the amplitudes, which depend on the characteristics of the pulse. At time t, we have

$$|\psi(t)\rangle = \sum_i \alpha_i e^{-iE_t/\hbar} e^{-\Gamma t/2} |e_i, 0\rangle + \sum_{f, \mathbf{k}\epsilon} C_{f, \mathbf{k}\epsilon}(t) |f, \mathbf{k}\epsilon\rangle,$$

where $\mathbf{k}\epsilon$ denotes the photon states. This says that the initial states $|e_i, 0\rangle$ have been damped at the rate $\Gamma = 1/\tau$ of spontaneous emission (τ is a common decay rate for all of the e_i substates). $C_{f, k\epsilon}(t)$ is the probability amplitude to find at time t the atom in the final state f with a photon of wave vector $\mathbf{k}$ and polarization ϵ. From the Wigner-Weisskopf theory of spontaneous emission, one finds

$$C_{f, \mathbf{k}\epsilon} = \sum_i C_{f, \mathbf{k}\epsilon}^{(i)}(t)$$

where

$$C_{f, \mathbf{k}\epsilon}^{(i)}(t) = \alpha_i E_{\mathbf{k}} \langle f | \epsilon \cdot \mathbf{D} | e_i \rangle e^{-i\mathbf{k}\cdot\mathbf{R}} \frac{e^{-i(E_f + \hbar ck)t/\hbar} - e^{-iE_i t/\hbar} e^{-\Gamma t/2}}{\hbar ck - (E_i - E_f) + i\hbar\Gamma/2}. \tag{11}$$

This is obtained by plugging $|\psi(t)\rangle$ into the Schrödinger equation and solving for $C_{f,\mathbf{k}\epsilon}$ in a system of coupled differential equations. In any case, $E_{\mathbf{k}}$ is the electric field of a photon at frequency $\hbar ck$ and $\mathbf{D}$ is the electric dipole operator of the atom. When $i = \{1, 2\}$, we find that $C_{f,\mathbf{k}\epsilon}$ is a sum of two terms, each corresponding to the emission from a given excited state $|e_i\rangle$. Each of these terms exhibits a resonance center around $\hbar ck = E_i - E_j$ with a width $\hbar\Gamma$. At resonance, each amplitude $C^{(i)}_{f,\mathbf{k}\epsilon}(t)$ is modulated at the Bohr frequency $E_i/\hbar$ if the corresponding excited state.

The average photon counting rate of the detector located at point $\mathbf{r}$ is equal to the expectation value at that point of the operator $E_{\mathbf{d}}^-(\mathbf{r})E_{\mathbf{d}}^+(\mathbf{r})$, which is the product of the positive and negative frequency parts of the electric field component along the direction $\mathbf{e_d}$. So, this quantity is given by

$$S(\mathbf{e_d}, \mathbf{r}, t) = \langle\psi(t)|\, E_d^-(\mathbf{r})E_{\mathbf{d}}^+(\mathbf{r})\,|\psi(t)\rangle.$$

Now, writing $E_{\mathbf{d}}^{\pm}(\mathbf{r})$ in terms of the normal modes of the electromagnetic field (this is where QED comes in)

$$E_d^+(\mathbf{r}) = \sum_{\mathbf{k}\epsilon} E_{\mathbf{k}}\epsilon_d a_{\mathbf{k}\epsilon}e^{i\mathbf{k}\cdot\mathbf{r}}.$$

$$E_d^-(\mathbf{r}) = \sum_{\mathbf{k}'\epsilon'} E_{\mathbf{k}'}\epsilon'_d a^{\dagger}_{\mathbf{k}'\epsilon'}e^{-i\mathbf{k}'\cdot\mathbf{r}}$$

where of course $a_{\mathbf{k}\epsilon}$ and $a^{\dagger}_{\mathbf{k}\epsilon}$ are annihilation and creation operators in mode $\mathbf{k}\epsilon$. With this, we find an expression for the signal:

$$S(\mathbf{e_d}, \mathbf{r}, t) = \sum_{\mathbf{k},\mathbf{k}',\epsilon,\epsilon'} \sum_f \sum_{i,j} E_{\mathbf{k}}E_{\mathbf{k}'}C^{(i)}_{f,\mathbf{k}\epsilon}(t)C^{(j)*}_{f,\mathbf{k}'\epsilon'}(t)\epsilon_d\epsilon'_d e^{i(\mathbf{k}-\mathbf{k}')\cdot\mathbf{r}}.$$

Finally, plugging Eq. 11 into this expression yields

$$
S(\mathbf{e_d}, \mathbf{r}, t) = \sum_{\mathbf{k},\mathbf{k'},\epsilon,\epsilon'} \sum_f \sum_{i,j} E_{\mathbf{k}} E_{\mathbf{k'}} \alpha_i E_{\mathbf{k}} \langle f | \epsilon \cdot \mathbf{D} | e_i \rangle e^{-i\mathbf{k}\cdot\mathbf{R}} \frac{e^{-i(E_f+\hbar ck)t/\hbar} - e^{-iE_it/\hbar} e^{-\Gamma t/2}}{\hbar ck - (E_i - E_f) + i\hbar\Gamma/2}
$$

$$
\times \left[\alpha_j E_{\mathbf{k'}} \langle f | \epsilon' \cdot \mathbf{D} | e_j \rangle e^{-i\mathbf{k'}\cdot\mathbf{R}} \frac{e^{-i(E_f+\hbar ck')t/\hbar} - e^{-iE_jt/\hbar} e^{-\Gamma t/2}}{\hbar ck' - (E_j - E_f) + i\hbar\Gamma/2} \right]^* \epsilon_d \epsilon'_d e^{i(\mathbf{k}-\mathbf{k'})\cdot\mathbf{r}}
$$

$$
= \sum_{\mathbf{k},\mathbf{k'},\epsilon,\epsilon'} \sum_f \sum_{i,j} E_{\mathbf{k}}^2 E_{\mathbf{k'}}^2 \langle f | \epsilon \cdot \mathbf{D} | e_i \rangle \alpha_i \alpha_j^* \langle e_j | \epsilon' \cdot \mathbf{D} | f \rangle \epsilon_d \epsilon'_d e^{i(\mathbf{k}-\mathbf{k'})\cdot(\mathbf{r}-\mathbf{R})}
$$

$$
\times \frac{e^{-i(E_f+\hbar ck)t/\hbar} - e^{-iE_it/\hbar} e^{-\Gamma t/2}}{\hbar ck - (E_i - E_f) + i\hbar\Gamma/2} \frac{e^{i(E_f+\hbar ck')t/\hbar} - e^{iE_jt/\hbar} e^{-\Gamma t/2}}{\hbar ck' - (E_j - E_f) - i\hbar\Gamma/2}.
$$

For simplicity, let $r_0 = |\mathbf{R} - \mathbf{r}|$ denote the distance between the atom and the detector, $k_0 = (E_e - E_f)/\hbar c$ is the average wavenumber of the detected optical transition, and $\omega_{ij} = (E_i - E_j)/\hbar$ is the Bohr frequency corresponding to the splitting between the states e_i and e_j, and $\theta(t - r_0/c)$ is the ordinary Heaviside function, equal to 1 if $t < r_o/c$ and to 0 otherwise, which allows for the propagation between the emitter and the detector. After non-trivial summing over all angular and energy parts, we find

$$
S(\mathbf{e_d}, \mathbf{r}, t) = \frac{1}{(4\pi\epsilon_0)^2} \frac{k_0^4}{r_0^2} \sum_f \sum_{i,j} \langle f | \mathbf{e_d D} | e_i \rangle \alpha_i \alpha_j^* \langle e_j | \mathbf{e_d D} | f \rangle
$$

$$
\theta\left(t - \frac{r_0}{c}\right) e^{-i\omega_{ij}\left(t - \frac{r_0}{c}\right)} e^{-\Gamma\left(t - \frac{r_0}{c}\right)}. \tag{12}
$$

Notice the inverse square law that arises. Now, the product of the amplitudes $\alpha_i \alpha_j^*$ are the matrix elements between the states $|e_i\rangle$ and $|e_j\rangle$ of the excited state density matrix $\rho_e(t)$ evaluated at time $t = 0$, i.e.,

$$
\alpha_i \alpha_j^* = \langle e_i | \rho_e(0) | e_j \rangle.
$$

So, assuming that r is fixed and that the retardation $r_0/c \approx 0$, we find that Eq. 12 becomes

$$
S(\mathbf{e_d}, t) = C \sum_{i,j} \left(e^{-i\omega_{ij}t} \langle e_i | \rho_e(0) | e_j \rangle e^{-\Gamma t} \right) \sum_f \langle e_j | \mathbf{e_d D} | f \rangle \langle f | \mathbf{e_d}^* \mathbf{D} | e_i \rangle \tag{13}
$$

where

$$
C = \frac{1}{(4\pi\epsilon_0)^2} \frac{k_0^4}{r_0^2}.
$$

Notice further that the first term in the expression above for S is just the density matrix element of ρ_e at time t, i.e.,

$$
e^{-i\omega_{ij}t} \langle e_i | \rho_e(0) | e_j \rangle e^{-\Gamma t} = \langle e_i | \rho_e(t) | e_j \rangle. \tag{14}
$$

As a result, we find

$$S(\mathbf{e_d}, t) = \sum_{i,j} \langle e_i | \, \rho_e(t) \, |e_j\rangle \, \langle e_j | \, \mathcal{L}(\mathbf{e_d}) \, |e_i\rangle = \sum_i \langle e_i | \, \rho_e(t) \mathcal{L}(\mathbf{e_d}) \, |e_i\rangle = \boxed{\mathrm{Tr}[\rho_e(t)\mathcal{L}(\mathbf{e_d})]} \quad (15)$$

where

$$\mathcal{L}(\mathbf{e_d}) = C \sum_f \mathbf{e_d} \mathbf{D} \, |f\rangle \, \langle f| \, \mathbf{e_d}^* \mathbf{D}.$$

So, we see that the fluorescence signal is the expectation value in the atomic excited states of a "detection" operator $\mathcal{L}(\mathbf{e_d})$, which is proportional to the component corresponding to the $e - f$ transition of the square of the atomic dipole projected along the detection polarization $\mathbf{e_d}$. Finally, to calculate explicitly the quantum beat signal, one has to know $\rho_e(t)$, which implies that one must know $\rho_e(0)$ since these are related by Eq. 14.

Three distinct time parameters are important for the description of the pulse: duration T (the pulse is assumed to interact with the atoms between time $t = -T$ and $t = 0$), its correlation time $\tau = 1/\Delta$, and its pumping time $T_p(t)$, which is inversely proportional to the instantaneous spectral density $u(\omega_0, t)$ of the pulse at the frequency ω_0 of the optical transition, and to the oscillation strength of the transition. It is defined as

$$\frac{1}{T_p(t)} = \frac{\pi}{\epsilon_0 \hbar^2} u(\omega_0, t) |\langle e| \, |D| \, |g\rangle|^2$$

where $\langle e| \, |D| \, |g\rangle$ is the radial part of the electric dipole matrix element between the states $|e\rangle$ and $|g\rangle$. $T_p(t)$ is the instantaneous average time between two successive photon absorptions from the pulse.

To derive rate equations for the evolution of the atomic system, we assume the broadline/short-pulse condition and the weak pumping condition given by

$$\Delta \gg \frac{1}{T_p(t)}.$$

We further assume that the following three conditions are satisfied:

$$\frac{1}{T} \gg \Gamma, \quad \frac{1}{T} \gg \omega_{ij}, \quad \Delta \gg \omega_{ij},$$

54

where ω_{ij} denotes the excited state frequency spacings. The first says that we can ignore spontaneous emission during the pulse itself. The second says that the pulse is short enough so that the atomic coherences do not have the time to precess during the pulse excitation. The last says that the pulse bandwidth is large enough to entirely cover the structure of the studied excited state.

In addition, we assume the Weak Pumping Limit, i.e., $T \ll T_p(t)$. This says that the pulse used to excited the atoms is weak enough so that it interacts linearly with the atomic system. In terms of photon processes, this means that at most one photon from the pulse is absorbed during time T. In this case, the evolution of the excited state density matrix is given by

$$\frac{d}{dt}\rho_e(t) = \frac{1}{T_p(t)}\frac{1}{G_g}\mathbf{P}_e\mathbf{e}_0\mathbf{DP}_g\mathbf{e}_0^*\mathbf{DP}_e,$$

where $\mathbf{e}_0$ is the polarization of the pulse. $\mathbf{P}_e = \sum_e |e\rangle\langle e|$, $\mathbf{P}_g = \sum_g |g\rangle\langle g|$ are the projectors into the excited and ground states, respectively. $\mathbf{G}_g$ is the degeneracy of the ground state. Integrating this equation gives

$$\rho_e(0) = \frac{K_0}{G_g}\mathbf{P}_e\mathbf{e}_0\mathbf{DP}_g\mathbf{e}_0^*\mathbf{DP}_e \tag{16}$$

where

$$K_0 = \int_{-T}^{0}\frac{dt}{T_p(t)},$$

is the time-integrated pumping rate. Eq. 16 is valid when the atomic ground state is not oriented prior to the pulse excitation. It says that the atomic density matrix components in the excited states are obtained as products of two amplitudes proportional to the atomic dipole matrix elements between the ground state and the relevant excited substates. Putting the expression for $\rho_e(0)$ in Eq. 16 into Eq. 13, we get

$$S(\mathbf{e_d}, t) = \frac{CK_0}{G_g}\sum_f\sum_{i,j}\sum_g \langle e_i|\mathbf{e}_0\mathbf{D}|g\rangle\langle g|\mathbf{e}_0^*\mathbf{D}|e_j\rangle\langle e_j|\mathbf{e}_d\mathbf{D}|f\rangle\langle f|\mathbf{e}_d^*\mathbf{D}|e_i\rangle e^{-\Gamma t}e^{-i\omega_{ij}t}.$$

More generally, it is possible that the ground state has some anisotropy before the pulse excitation. This requires us to modify Eq. 16 to account for te anisotropy of the atom in the state g:

$$\rho_e(0) = K_0\mathbf{P}_e\mathbf{e}_0\mathbf{DP}_g\rho_g(-T)\mathbf{P}_g\mathbf{e}_0^*\mathbf{DP}_e, \tag{17}$$

55

where $\rho_g(-T)$ is the density matrix in state g at time $-T$ before the pulse. To derive this, we can assume that the ground state has no time to evolve between the times $-T$ and 0, so that $\rho_g(-T)$ can be replaced by $\rho_g(0)$. In this case, the density matrix of the excited states $\rho_e(t)$ satisfies

$$
\begin{aligned}
\langle e_i | \rho_e(t) | e_j \rangle &= e^{-i\omega_{ij}t} e^{-\Gamma t} \langle e_i | \rho_e(0) | e_j \rangle \\
&= e^{-i\omega_{ij}t} e^{-\Gamma t} \langle e_i | K_0 \mathbf{P}_e \mathbf{e}_0 \mathbf{D} \mathbf{P}_g \rho_g(-T) \mathbf{P}_g \mathbf{e}_0^* \mathbf{D} \mathbf{P}_e | e_j \rangle \\
&= e^{-i\omega_{ij}t} e^{-\Gamma t} K_0 \sum_{jj',gg'} \langle e_i | e_j \rangle \langle e_j | \mathbf{e}_0 \mathbf{D} | g \rangle \langle g | \rho_g(-T) | g' \rangle \langle g' | \mathbf{e}_0^* \mathbf{D} | e_{j'} \rangle \langle e_{j'} | e_j \rangle \\
&= e^{-i\omega_{ij}t} e^{-\Gamma t} K_0 \sum_{gg'} \langle e_i | \mathbf{e}_0 \mathbf{D} | g \rangle \langle g | \rho_g(-T) | g' \rangle \langle g' | \mathbf{e}_0^* \mathbf{D} | e_j \rangle.
\end{aligned}
$$

Plugging this into Eq. 15 we find

$$
\begin{aligned}
S(\mathbf{e_d}, t) &= \sum_{i,j} \langle e_i | \rho_e(t) | e_j \rangle \langle e_j | \mathcal{L}(\mathbf{e_d}) | e_i \rangle \\
&\propto \sum_{i,j} e^{-i\omega_{ij}t} e^{-\Gamma t} \sum_{gg'} \langle e_i | \mathbf{e}_0 \mathbf{D} | g \rangle \langle g | \rho_g(-T) | g' \rangle \langle g' | \mathbf{e}_0^* \mathbf{D} | e_j \rangle \langle e_j | \mathcal{L}(\mathbf{e_d}) | e_i \rangle \\
&\propto \sum_{i,j,f,g,g'} e^{-i\omega_{ij}t} e^{-\Gamma t} \langle e_i | \mathbf{e}_0 \mathbf{D} | g \rangle \langle g | \rho_g(-T) | g' \rangle \langle g' | \mathbf{e}_0^* \mathbf{D} | e_j \rangle \langle e_j | \mathbf{e_d} \mathbf{D} | f \rangle \langle f | \mathbf{e_d}^* \mathbf{D} | e_i \rangle.
\end{aligned}
$$

(18)

This corresponds exactly to Eq. 4 in Section 2.3.3.

6.2 Graphical methods for angular momentum calculations [9]

This is a very quick guide to the graphic methods for solving angular-momentum problems. As a result, most of the mathematics behind these rules will be neglected. For more details, please refer to [9].

6.2.1 The basics

First, the $3j$-symbol can be represented by Figure 20

The symmetry relation

$$
\begin{pmatrix} a & b & c \\ \alpha & \beta & \gamma \end{pmatrix} = (-1)^{a+b+c} \begin{pmatrix} a & c & b \\ \alpha & \gamma & \beta \end{pmatrix}
$$

Figure 20: The graphical Wigner $3j$-symbol [9]

Figure 21: Symmetry relation for the graphical Wigner $3j$-symbol [9]

implies Figure 21

The sign $+/-$ at the node denotes the counterclockwise/clockwise orientation. The associated $3j$-symbol does not change under deformations of a diagram so long as such deformations do not alter the diagram's orientation. Next, sometimes we see various phase factors of the form $(-1)^{x+y+z+\cdots}$. These are represented by arrows. In particular, we have Figure 22

Figure 22: Phase factor as an arrow [9]

More complicated diagrams maybe constructed by putting these ingredients together. Two lines representing the same total angular momentum can be joined. Joining two lines implies that the z-components of the two angular momenta should be set equal and summed over. We will usually omit the z-components of angular momenta from diagrams.

With these rules we should be able to write down any Clebsch-Gordan coefficient in terms of $3j$-symbols. What we'll focus on next is the Wigner $6j$-symbol, which is given by Figure 23, where the sum is taken over all magnetic quantum numbers.

$$\begin{Bmatrix} a & b & e \\ d & c & f \end{Bmatrix} = \sum (-)^{a+e+c-\alpha-\epsilon-\gamma} \begin{pmatrix} a & f & c \\ \alpha & \phi & -\gamma \end{pmatrix} \begin{pmatrix} c & d & e \\ \gamma & \delta & -\epsilon \end{pmatrix} \begin{pmatrix} e & b & a \\ \epsilon & \beta & -\alpha \end{pmatrix} \begin{pmatrix} b & d & f \\ \beta & \delta & \phi \end{pmatrix}$$

Figure 23: The graphical Wigner $6j$-symbol [9]

6.2.2 Rules for transforming graphs

Often in calculations, we start with an algebraic expression and translate it into a rather complicated graphical representation. To continue with the calculation, we often must transform the complicated graph into products of more elementary ones before this simpler graph is converted back into a simplified algebraic expression. Here are some rules to perform the transformations.

First, we must know how to add/remove arrows or change their directions. There are **five** rules. The first four rules are best shown in diagrams (see Figures 24, 25, 26, 27). The

Figure 24: Two opposite arrows "cancel" [9]

Figure 25: Two arrows in the same direction "cancel" and give a phase [9]

fifth rule says that the direction of all arrows and the signs of all nodes may be changed simultaneously in a closed diagram without altering the value of the diagram. The proof for this rule is once again in [9].

$$\underset{a\alpha}{\longrightarrow} \quad \underset{a\alpha'}{\quad} \; = \; (-)^{2a} \; \underset{a\alpha}{\longleftarrow} \quad \underset{a\alpha'}{\quad}$$

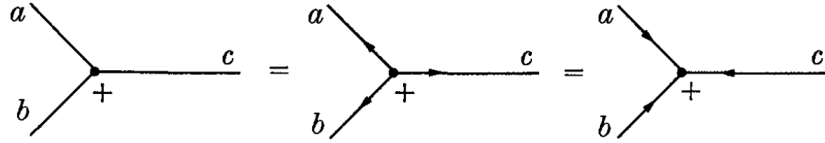Figure 26: Changing the direction of an arrow gives a phase [9]

Figure 27: 3 arrows (*all* away from or towards the node) might be added to the diagram [9]

Second, we must know how to "factor" a complicated diagram into smaller, more recognizable ones. This brings us to the the Three Theorems for Block Diagrams in [9], but we'll just learn the rules by looking at some model diagrams. One important result is that if we denote a block F with n external lines by Figure 28, then Figure 29 follows.

$$F_n\begin{pmatrix} j_1 \cdots j_n \\ m_1 \ldots m_n \end{pmatrix} =$$

Figure 28: From [9]

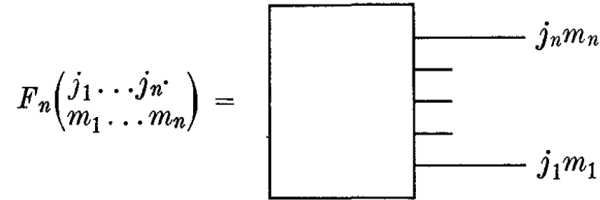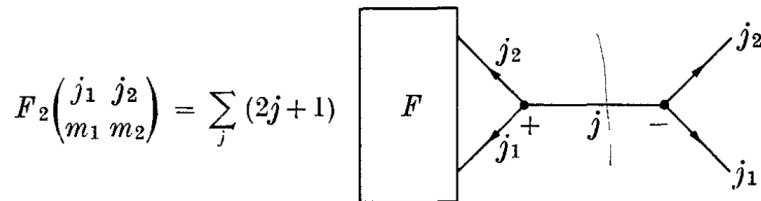$$F_2\begin{pmatrix} j_1 & j_2 \\ m_1 & m_2 \end{pmatrix} = \sum_j (2j+1) \quad F$$

Figure 29: From [9]

We focus on the cases where there are two (Figure 30) and three (Figure 31) connecting
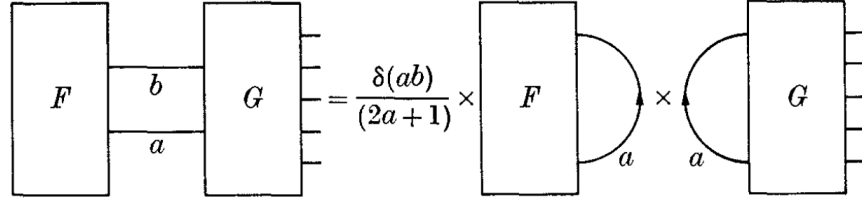
59

lines between two blocks.

Figure 30: Two blocks with two connecting lines [9]
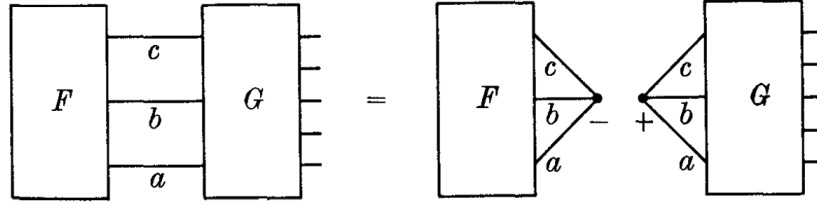
Figure 31: Two blocks with three connecting lines [9]

In the case where we have a single block with 2 or 3 external lines, we can simply call this block F and let the block G be blank. By doing so, we can treat the external lines of block F as connecting lines and apply the rules. For example, we can prove the relation

$$\sum_{\delta\epsilon\phi} \begin{pmatrix} d & e & c \\ -\delta & \epsilon & \gamma \end{pmatrix} \begin{pmatrix} e & f & a \\ -\epsilon & \phi & \alpha \end{pmatrix} \begin{pmatrix} f & d & b \\ -\phi & \delta & \beta \end{pmatrix} (-1)^{d+e+f-\delta-\epsilon-\phi} = \begin{Bmatrix} a & b & c \\ d & e & f \end{Bmatrix} \begin{pmatrix} a & b & c \\ \alpha & \beta & \gamma \end{pmatrix}$$

graphically in Figure 32.

Another interesting example is calculating the block in Figure 33, which can be transformed into Figure 34. Here, we have used the sequence of transformation shown in Figure 35.

60

Figure 32: An example of using the block-diagram theorems [9]

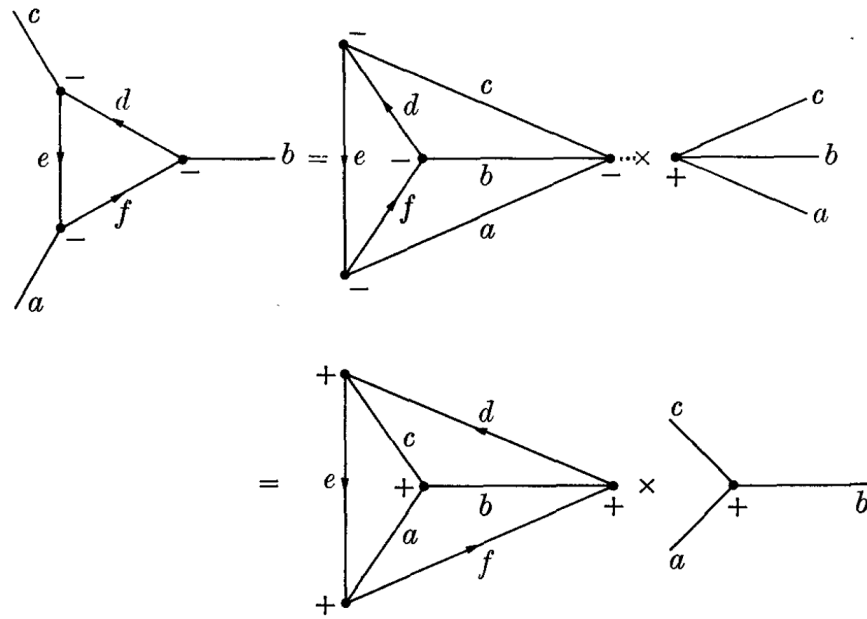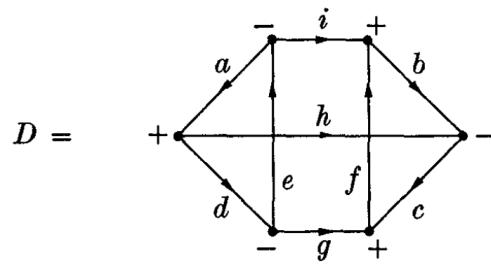

Figure 33: From [9]

$$= \begin{Bmatrix} g\ h\ i \\ a\ e\ d \end{Bmatrix} \begin{Bmatrix} g\ h\ i \\ b\ f\ c \end{Bmatrix}$$
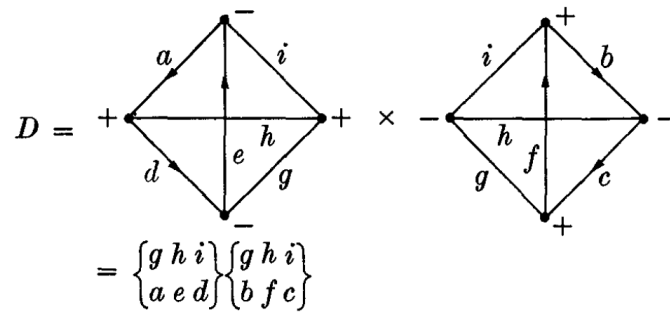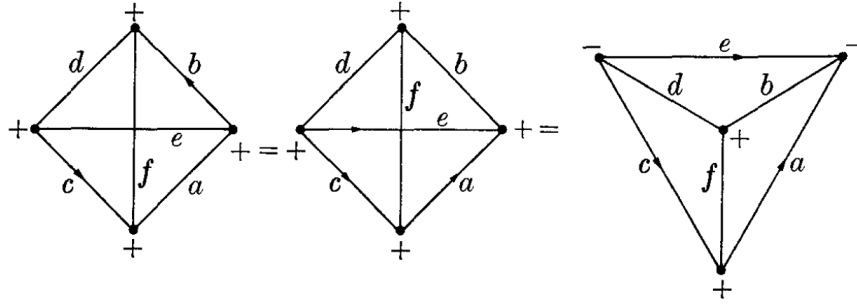
Figure 34: From [9]

Figure 35: From [9]

6.2.3 Calculating $X(F_e, F'_e, F_i, F_f; p_0, p'_0, p, p')$

We're now ready to calculate $X(F_e, F'_e, F_i, F_f; p_0, p'_0, p, p')$ in Section 2.3.3. Recall that:

$$X(F_e, F'_e, F_i, F_f; p_0 \cdot p'_o, p, p') = \sum_{\substack{M_e M'_e \\ M_i M_f}} (-1)^{F_e - M_e + F'_e - M'_e + F_i - M_i + F_f - M_f} \begin{pmatrix} F_e & 1 & F_i \\ -M_e & p_0 & M_i \end{pmatrix}$$

$$\times \begin{pmatrix} F_i & 1 & F'_e \\ -M_i & p'_0 & M'_e \end{pmatrix} \begin{pmatrix} F'_e & 1 & F_f \\ -M'_e & p & M_f \end{pmatrix} \begin{pmatrix} F_f & 1 & F_e \\ -M_f & p' & M_e \end{pmatrix}.$$

By using the graphical representations for the $3j$-symbol and an arrow, the term

$$(-1)^{F_e - M_e} \begin{pmatrix} F_e & 1 & F_i \\ -M_e & p_0 & M_i \end{pmatrix}$$

is represented by the graph in Figure 36.
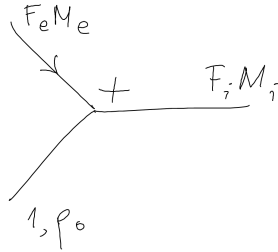
Figure 36: $3j$-symbol and arrow

Putting the four terms in X together by joining lines we get to Figure 37. We can treat Figure 37 as a two-block diagram with two connecting lines. Applying the block-diagram

theorem, we obtain Figure 38. To simplify Figure 38 further, we add three diverging arrows to the node $k - F_e - F_e'$ and invoke the "external line rule" used in Figure 32. This gives Figure 39. Next, to the left-most term, add diverging arrows to the $F_i - F_e - 1$ node and
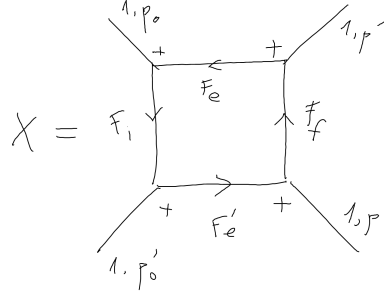
Figure 37: X
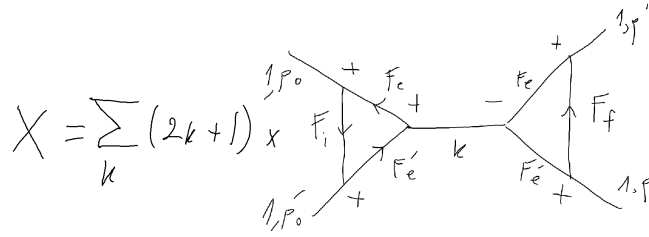
Figure 38: X
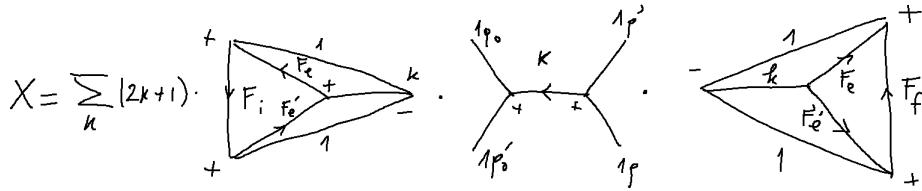
Figure 39: X

converging arrows to the $1 - F_e' - F_i$ node. This has no effect on the F_i line. However, the arrows on the F_e and F_e' lines get canceled, and we gain new arrows on the "outer" 1-lines. Repeat this process for the right-most term so that its "inner arrows" also get canceled. Notice further that switching arrow directions on the 1-line doesn't do anything to the graph because the phase $(-1)^{2\times 1} = 1$. Using this fact, we can also change the orientations

of the nodes with the $-$ sign so that they become $+$. After some extra careful changing of signs and arrow directions, we will find the "triangular terms" in the correct form for the $6j$-symbol. We also recognize that the term in the middle is just the product of two $3j$-symbols. So, in the end, we write

$$X(F_e, F'_e, F_i, F_f; p_0.p'_o, p, p') = \sum_{kq}(2k+1)(-1)^{q+2F_f-F_e-F'_e} \begin{pmatrix} 1 & 1 & k \\ p_0 & p'_0 & q \end{pmatrix} \begin{pmatrix} 1 & 1 & k \\ p & p' & -q \end{pmatrix}$$
$$\times \begin{Bmatrix} F_i & F_e & 1 \\ k & 1 & F'_e \end{Bmatrix} \begin{Bmatrix} 1 & k & 1 \\ F_e & F_f & F'_e \end{Bmatrix}.$$

6.2.4   Calculating $Y(F_e, F'_e; k)$ and $Z(F_e, F'_e; k)$

Recall their formulas from Section 2.3.3:

$$Y(F_e, F'_e; k) = \sum_{F_i}(2F_i+1)(-1)^{2J_e+k+F_e+F'_e+I+J_i+F_i} \begin{Bmatrix} F_e & F_i & 1 \\ J_i & J_e & I \end{Bmatrix} \begin{Bmatrix} F'_e & F_i & 1 \\ 1 & k & F_e \end{Bmatrix} \begin{Bmatrix} I & F_i & J_i \\ 1 & J_e & F'_e \end{Bmatrix}.$$

and

$$Z(F_e, F'_e; k) = \sum_{F_f}(2F_f+1)(-1)^{2J_e+k+F_e+F'_e+I+J_f+F_f} \begin{Bmatrix} F'_e & F_f & 1 \\ J_f & J_e & I \end{Bmatrix} \begin{Bmatrix} F_e & F_f & 1 \\ 1 & k & F'_e \end{Bmatrix} \begin{Bmatrix} I & F_f & J_f \\ 1 & J_e & F_e \end{Bmatrix}.$$

We will perform these calculations based on Example 7 of Chapter VII: Graphical Methods in Angular Momentum in [9]. It suffices to just do the Y calculation. The result for Z can be obtained by a simple change of variables. To start, we look at Example 7, which says that

$$\sum_x(2x+1)(-1)^{a+b+c+d+e+f+g+h+i+x} \begin{Bmatrix} e & f & x \\ b & a & i \end{Bmatrix} \begin{Bmatrix} a & b & x \\ c & d & h \end{Bmatrix} \begin{Bmatrix} d & c & x \\ f & e & g \end{Bmatrix} = \begin{Bmatrix} g & h & i \\ a & e & d \end{Bmatrix} \begin{Bmatrix} g & h & i \\ b & f & c \end{Bmatrix}.$$

We want to do some permutations to the $6j$-symbols in Y so that it matches the expression above. We first recognize that F_i plays the role of x.

$$Y(F_e, F'_e; k) = \sum_{F_i}(2F_i+1)(-1)^{2J_e+k+F_e+F'_e+I+J_i+F_i} \begin{Bmatrix} F_e & 1 & F_i \\ J_i & I & J_e \end{Bmatrix} \begin{Bmatrix} I & J_i & F_i \\ 1 & F'_e & J_e \end{Bmatrix} \begin{Bmatrix} F'_e & 1 & F_i \\ 1 & F_e & k \end{Bmatrix}$$
$$= \begin{Bmatrix} k & J_e & J_e \\ I & F_e & F'_e \end{Bmatrix} \begin{Bmatrix} k & J_e & J_e \\ J_i & 1 & 1 \end{Bmatrix}.$$

For Z, we observe that F_e and F'_e are exchanged, J_i is replaced by J_f, and that F_f plays the role of x. But since the $6j$-symbol is invariant under permutations of columns, the $F_e - F'_e$ exchange in fact has no effect. So,

$$Z(F_e, F'_e; k) = \begin{Bmatrix} k & J_e & J_e \\ I & F'_e & F_e \end{Bmatrix} \begin{Bmatrix} k & J_e & J_e \\ J_f & 1 & 1 \end{Bmatrix} = \begin{Bmatrix} k & J_e & J_e \\ I & F_e & F'_e \end{Bmatrix} \begin{Bmatrix} k & J_e & J_e \\ J_f & 1 & 1 \end{Bmatrix}.$$

To see how one might do this graphically, we observe that

$$\sum_x (2x + 1)(-1)^{a+b+c+d+e+f+g+h+i+x} \begin{Bmatrix} e & f & x \\ b & a & i \end{Bmatrix} \begin{Bmatrix} a & b & x \\ c & d & h \end{Bmatrix} \begin{Bmatrix} d & c & x \\ f & e & g \end{Bmatrix}$$

can be written as Figure 40 [9]. To obtain this result, we just write out the $6j$-symbols
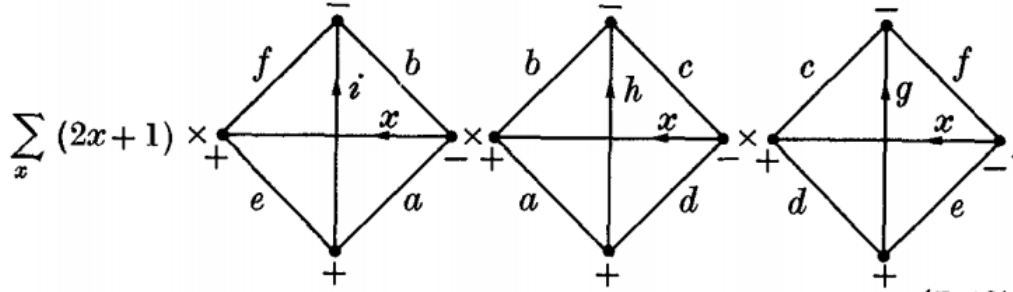
Figure 40: From [9]

as the "triangular" graphs as before. Next, the phase factors will change some of the orientations, which convert from $+$ nodes to $-$ and move the "inner node" outside of the triangle, turning it into a square. Next, the graph in Figure 40 [9] can be "contracted" into the graph in Figure 42. To go from Figure 40 to Figure 42, we use the Block-Diagram Theorems and join the 3 graphs into the form in Figure 41 [9], which can then be separated on the lines (ghi) to give Figure 42. After some change of orientations at the nodes of Figure 42 we get the desired result:

$$\begin{Bmatrix} g & h & i \\ a & e & d \end{Bmatrix} \begin{Bmatrix} g & h & i \\ b & f & c \end{Bmatrix}.$$

65
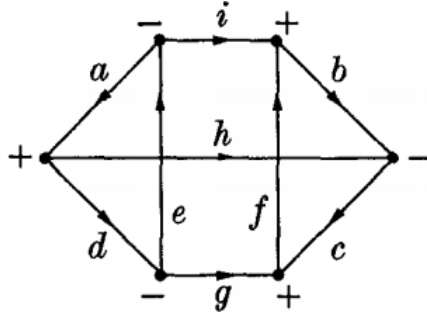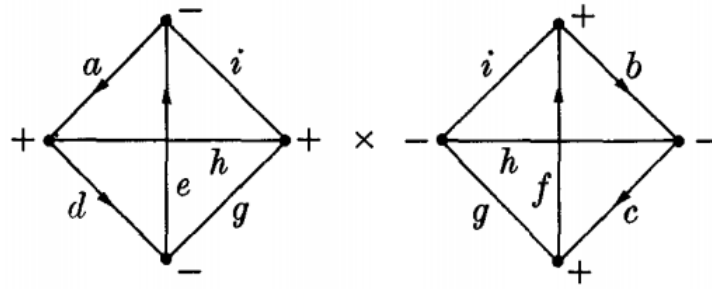
Figure 41: From [9]

Figure 42: From [9]

6.3 Spherical Basis and the Wigner $\mathcal{D}$-matrix

A spherical basis is the basis used to express spherical tensors. Spherical bases are ubiquitous in angular-momentum problems in quantum mechanics. While spherical polar coordinates are one orthogonal coordinate system for expressing vectors and tensors using polar and azimuthal angles and radial distance, the spherical basis are constructed from the standard basis and use complex numbers. In three dimensions, a vector $\mathbf{A}$ in the standard basis can be written as

$$\mathbf{A} = A_x \mathbf{e}_x + A_y \mathbf{e}_y + A_z \mathbf{e}_z.$$

where the coordinates A_i can be complex. In the spherical basis denoted $\mathbf{e}_+, \mathbf{e}_-, \mathbf{e}_0$,

$$\mathbf{A} = A_+ \mathbf{e}_+ + A_- \mathbf{e}_- + A_0 \mathbf{e}_0$$

where

$$\mathbf{e}_\pm = \mp \frac{1}{\sqrt{2}} (\mathbf{e}_x \pm i \mathbf{e}_y)$$

66

and

$$\mathbf{e}_0 = \mathbf{e}_z.$$

This change of basis can be captured by

$$\begin{pmatrix} \mathbf{e}_+ \\ \mathbf{e}_- \\ \mathbf{e}_0 \end{pmatrix} = \mathbf{U} \begin{pmatrix} \mathbf{e}_x \\ \mathbf{e}_y \\ \mathbf{e}_z \end{pmatrix} = \begin{pmatrix} -1/\sqrt{2} & -i/\sqrt{2} & 0 \\ +1/\sqrt{2} & -i/\sqrt{2} & 0 \\ 0 & 0 & 1 \end{pmatrix} \begin{pmatrix} \mathbf{e}_x \\ \mathbf{e}_y \\ \mathbf{e}_z \end{pmatrix}.$$

The corresponding change of coordinates is

$$\begin{pmatrix} A_+ \\ A_- \\ A_0 \end{pmatrix} = \mathbf{U}^* \begin{pmatrix} A_x \\ A_y \\ A_z \end{pmatrix}.$$

We notice that U is unitary, i.e., $U^\dagger = U^{-1}$.

A general spherical tensor transforms under a rotation the same way spherical harmonics transform. It turns out that if T_q^k is a spherical tensor, then

$$\mathcal{D}(\mathbf{R})T_q^k \mathcal{D}^\dagger(\mathbf{R}) = \sum_{q'=-k}^{k} T_{q'}^k \mathcal{D}_{qq'}^k(\mathbf{R}) \tag{19}$$

where $\mathbf{R}$ is a 3-dimensional rotation operator and $\mathcal{D}$ is the Wigner $\mathcal{D}$-matrix associated with the rotation matrix $\mathbf{D}$. With corresponding Euler angles α, β, γ, $\mathbf{R}$ can be written as

$$\mathbf{R}(\alpha, \beta, \gamma) = e^{-i\alpha\sigma_z} e^{-i\beta\sigma_y} e^{-i\gamma\sigma_z}.$$

The Euler angles are characterized by the keywords: $z - y - z$ convention, right-handed frame, right-hand screw rule, active interpretation. Here σ_i are the Pauli matrices, which are also generators of the Lie algebra of SO(3). Let's unpack the right-hand side of Eq. 19. $\mathcal{D}$ is a unitary square matrix of dimension $2k + 1$ in this spherical basis with elements $\mathcal{D}_{qq'}^k(\mathbf{R})$, defined by

$$\mathcal{D}_{qq'}^k(\alpha, \beta, \gamma) \equiv \langle kq| \, \mathbf{R}(\alpha, \beta, \gamma) \, |kq'\rangle = e^{-iq\alpha} \, \langle kq| \, e^{-i\beta\sigma_y} \, |kq'\rangle \, e^{-iq'\gamma} = e^{-iq\alpha} \mathcal{D}_{qq'}^j(0, \beta, 0) e^{-iq'\gamma}.$$

Here $\mathcal{D}_{qq'}^j(0, \beta, 0)$ is referred to as the **Wigner's (small) d-matrix**:

$$d_{qq'}^k(\beta) = \mathcal{D}_{qq'}^j(0, \beta, 0).$$

Elements of $d_{qq'}^k(\beta)$ can be readily found. In the case where $k = 2$ and $q = q' = 0$, we have

$$d_{00}^2(\beta) = \frac{1}{2}(3\cos^2\beta - 1) = P_2(\cos\beta).$$

It turns out that

$$\mathcal{D}_{00}^k(\varphi, \theta, \phi) = P_k(\cos\theta)$$

where $P_k(x)$ are Legendre polynomials. In general,

$$\mathcal{D}_{m0}^l(\alpha, \beta, \gamma) = \sqrt{\frac{(l-m)!}{(l+m)!}}P_l^m(\cos\beta)e^{-im\alpha},$$

which implies that

$$d_{m0}^l(\beta) = \sqrt{\frac{(l-m)!}{(l+m)!}}P_l^m(\cos\beta).$$

Here, $P_l^m(x)$ are the associated Legendre polynomials.

6.4 Zeeman hyperfine splitting MATLAB code

```
% looking at 5P3/2 in K39

clear

J = 3/2;
I = 3/2;
L = 1;
S = 1/2;
B = 0:0.01:1.5; % units is Gauss
Ahf = 1.973e6; % Ahf coef in Hz
Bhf = 0.870e6; % Bhf coef in Hz

mJ = J:-1:-J;
mI = I:-1:-I;

size = length(mJ)*length(mI);
H = zeros(size, size);

% creat a basis for the Hamiltonian
basis = [];
for mj = mJ
    for mi = mI
        basis = [basis; [mj mi]];
```

```
    end
end


zeeman = figure(1);
for b = B % loop over field strengths
    % create the Hamiltonian, element-by-element
    % I'm not imposing the symmetric condition on H to make it easy to code
    % The formulas for the matrix elements take care of H's self-adjointness
    for r = 1:size
        mj = basis(r,1);
        mi = basis(r,2);
        for c = 1:size
            mjj = basis(c,1);
            mii = basis(c,2);


            H(r,c) = Ahf*A_hfs(J, I, mj, mi, mjj, mii)...
                + Bhf*B_hfs(J, I, mj, mi, mjj, mii)...
                + mag(b, J, L, S, mj, mi, mjj, mii);
        end
    end
    % diagonalize and plot eigenvalues associated with field strength b
    energies = eig(H)/1e6; % fix units to MHz
    hold on
    plot(b*ones(size), energies, 'o', 'Color', 'red', 'MarkerSize',1);
end
hold off
title('Hyperfine Zeeman splitting')
xlabel('Magnetic Field (G)')
ylabel('Energy Shift (MHz)')

%%%%%% FUNCTIONS %%%%%%
% This part is self-explanatory, so I won't add further comments

function Ahfs = A_hfs(J, I, mj, mi, mjj, mii)
    Ahfs = 0;
    if mj == mjj && mi == mii
        Ahfs = mj*mi;
    elseif mj == mjj + 1 && mi == mii - 1
        Ahfs = (1/2)*sqrt((J+mj)*(J-mj+1)*(I-mi)*(I+mi+1));
    elseif mj == mjj - 1 && mi == mii + 1
        Ahfs = (1/2)*sqrt((J-mj)*(J+mj+1)*(I+mi)*(I-mi+1));
    else
        Ahfs = 0;
```

```
    end
end

function Bhfs = B_hfs(J, I, mj, mi, mjj, mii)
    Bhfs = 0;
    if mj == mjj && mi == mii
        Bhfs = (1/2)*(3*mi^2-I*(I+1))*(3*mj^2-J*(J+1));
    elseif mj == mjj - 1 && mi == mii + 1
        Bhfs = (3/4)*(2*mjj-1)*(2*mii+1)*sqrt((J+mjj)*(J-mjj+1)*(I-mii)*(I+mii+1));
    elseif mj == mjj + 1 && mi == mii - 1
        Bhfs = (3/4)*(2*mjj+1)*(2*mii-1)*sqrt((J-mjj)*(J+mjj+1)*(I+mii)*(I-mii+1));
    elseif mj == mjj - 2 && mi == mii + 2
        Bhfs = (3/4)*sqrt((J+mjj)*(J+mjj-1)*(J-mjj+1)*(J-mjj+2)...
            *(I-mii)*(I-mii-1)*(I+mii+1)*(I+mii+2));
    elseif mj == mjj + 2 && mi == mii - 2
        Bhfs = (3/4)*sqrt((J-mjj)*(J-mjj-1)*(J+mjj+1)*(J+mjj+2)...
            *(I+mii)*(I+mii-1)*(I-mii+1)*(I-mii+2));
    else
        Bhfs = 0;
    end
    Bhfs = Bhfs/(2*I*(2*I-1)*J*(2*J-1));
end

function mag = mag(B, J, L, S, mj, mi, mjj, mii)
    me = 9.1093837015e-31; % electron mass
    mn = 1.67493e-27; % neutron mass
    eC = 1.60218e-19; % electric charge
    hbar = 1.054571817e-34;
    muB = eC*hbar/(2*me); % Bohr magneton
    gL = 1 - me/mn; % gyro magnetic factor of the orbital
    gS = 2.0023193043622; % electron spin g-factor
    gJ = gL*(J*(J+1)-S*(S+1)+L*(L+1))/(2*J*(J+1))
        + gS*(J*(J+1)+S*(S+1)-L*(L+1))/(2*J*(J+1));
    gI = -0.00014193489; % this is an experimental value


    mag = 0;
    if mj == mjj && mi == mii
        mag = (muB/hbar)*(gJ*mj + gI*mi)*B*1e-4; % B is in Gauss
    else
        mag = 0;
    end
end
```

References

[1] A. Mills, J. A. Behr, L. A. Courneyea, and M. R. Pearson. Lifetime of the potassium $5p_{12}$ state. *Phys. Rev. A*, 72:024501, Aug 2005.

[2] R.W. Berends, W. Kedzierski, J.B. Atkinson, and L. Krause. The radiative lifetimes of the potassium 5p, 6p and 7p states. *Spectrochimica Acta Part B: Atomic Spectroscopy*, 43(9):1069–1073, 1988.

[3] U. I. Safronova and M. S. Safronova. High-accuracy calculation of energies, lifetimes, hyperfine constants, multipole polarizabilities, and blackbody radiation shift in ^{39}K. *Phys. Rev. A*, 78:052504, Nov 2008.

[4] S Svanberg. Natural lifetimes and hyperfine structure for ^{39}k in the $5p_{3/2}$ and $6p_{3/2}$ levels of the ki spectrum by resonance scattering of light. *Physica Scripta*, 4(6):275–279, Dec 1971.

[5] J. Ney. Hyperfeinstrukturuntersuchung der 4p und $5p_{3/2}$-terme im k i-spektrum durch resonanzstreuung von licht zur bestimmung der kernquadrupolmomente von ^{39}k und ^{41}k. *Zeitschrift für Physik A Hadrons and nuclei*, 223(2):126–138, Apr 1969.

[6] Robert W. Schmieder, Allen Lurio, and W. Happer. Hyperfine structure and lifetimes of the $4p_{3/2}$ and $5p_{3/2}$ states of ^{39}k. *Phys. Rev.*, 173:76–79, Sep 1968.

[7] Kimball D. F. Budker D. and DeMille D. P. *Atomic physics: An exploration through problems and solutions.* Oxford University Press, 2004.

[8] S. Haroche and ed K. Shimoda. *Topics in Applied Physics, vol 13, High Resolution Laser Spectroscopy.* Berlin: Springer Verlag, 1976.

[9] Brink D. M. and Satchler G. R. *Angular Momentum.* Oxford: Clarendon, 1971.

[10] R Luypaert and J Van Craen. Hyperfine-structure quantum beats: application of the graphical methods of angular-momentum theory to the calculation of intensity profiles. *Journal of Physics B: Atomic and Molecular Physics*, 10(18):3627–3636, dec 1977.

[11] David McKay. Potassium 5p line data. 2009.

[12] E. Arimondo, M. Inguscio, and P. Violino. Experimental determinations of the hyperfine structure in the alkali atoms. *Rev. Mod. Phys.*, 49:31–75, Jan 1977.

[13] J Simsarian, Luis Orozco, G Sprouse, and W Zhao. Lifetime measurements of the 7p levels of atomic francium. (57), 1998-01-01 1998.

[14] D. Sheng, A. Pérez Galván, and L. A. Orozco. Lifetime measurements of the $5d$ states of rubidium. *Phys. Rev. A*, 78:062506, Dec 2008.

[15] Constantine E. Theodosiou. Lifetimes of alkali-metal—atom rydberg states. *Phys. Rev. A*, 30:2881–2909, Dec 1984.

[16] Norman Ramsey. *Molecular beams*. Oxford University Press, 1985.

[17] L. Leblanc. The hyperfine structure of potassium-40. 2006. https://ultracold.physics.utoronto.ca/reprints/LeBlanc40K.pdf.

[18] Andrew J Orr-Ewing and Richard N Zare. Orientation and alignment of reaction products. *Annual Review of Physical Chemistry*, 45(1):315–366, 1994.

[19] Philip Michael Adamson. Resonant collisions of potassium atoms. *Colby Honors Theses*, 2016.

[20] PicoQuant. Timeharp 260 data sheet. https://www.picoquant.com/images/uploads/downloads/timeharp260.pdf.

[21] L. Young, W. T. Hill, S. J. Sibener, Stephen D. Price, C. E. Tanner, C. E. Wieman, and Stephen R. Leone. Precision lifetime measurements of cs 6p $^2p_{1/2}$ and 6p $^2p_{3/2}$ levels by single-photon counting. *Phys. Rev. A*, 50:2174–2181, Sep 1994.

[22] B. P. Kibble, G. Copley, and L. Krause. Effect of imprisonment of radiation in sodium vapor on the measured lifetime of the 3^2p states. *Phys. Rev.*, 153:9–12, Jan 1967.